Low-temperature thermocatalytic removal of formaldehyde in air using copper manganite spinels

Yongbiao Hua [a], Kumar Vikrant [a], Ki-Hyun Kim [a, *], Philippe M. Heynderickx [b, c, *], Danil W. Boukhvalov [d, e]

[a] Department of Civil and Environmental Engineering, Hanyang University, 222 Wangsimni-Ro, Seoul 04763, Republic of Korea

[b] Center for Environmental and Energy Research (CEER), Engineering of Materials via Catalysis and Characterization, Ghent University Global Campus, 119-5 Songdo Munhwa-ro, Yeonsu-gu, Incheon 406-840, Republic of Korea

[c] Department of Green Chemistry and Technology, Faculty of Bioscience Engineering, Ghent University, Coupure Links 653, B-9000 Ghent, Belgium

[d] College of Science, Institute of Materials Physics and Chemistry, Nanjing Forestry University, Nanjing 210037, China

[e] Institute of Physics and Technology, Ural Federal University, Mira Street 19, 620002 Yekaterinburg, Russia

Abstract

The removal of formaldehyde (FA) is vital for indoor air quality management in light of its carcinogenic propensity and adverse environmental impact. A series of copper manganite spinel structures (e.g., $CuMn_2O_4$) are prepared using the sol-gel combustion method and treated with reduction or oxidation pretreatment methods at 300°C condition. Accordingly, $CuMn_2O_4$-O ("O" suffix for oxidation pre-treatment in air) is identified as the best performer to achieve 100% conversion (X_{FA}) of FA (50 ppm) at 90°C; its performance, if assessed in terms of reaction kinetic rate (r) at X_{FA} =10%, is 5.02E-03 mmol g^{-1} h^{-1}. The FA removal performance increases systematically with decreases in flow rate, FA concentration, and relative humidity (RH) or with increases in bed mass. The reaction pathways and intermediates of FA catalytic oxidation on $CuMn_2O_4$-A are studied with density functional theory simulations, temperature-programmed characterization experiments, and *in-situ* diffuse reflectance infrared Fourier transform spectroscopy. The synergistic combination of large quantities of adsorbed oxygen (O_A) species and oxidized metal species (e.g., Cu^{2+}) contribute to the enhanced catalytic performance of $CuMn_2O_4$-O to oxidize FA into CO_2 with the reaction intermediates of H_2CO_2 (DOM), $HCOO^-$, and CO. The present study is expected

to provide valuable insights into the thermocatalytic oxidation of FA over spinel $CuMn_2O_4$ materials and their catalytic performances in relation to the key process variables.

Keywords: Formaldehyde; Volatile organic compounds; Catalytic oxidation; copper manganite spinel

*Correspondence: kkim61@hanyang.ac.kr (K.-H. Kim); philippe.heynderickx@ghent.ac.kr (P. M. H.)

Graphical abstract

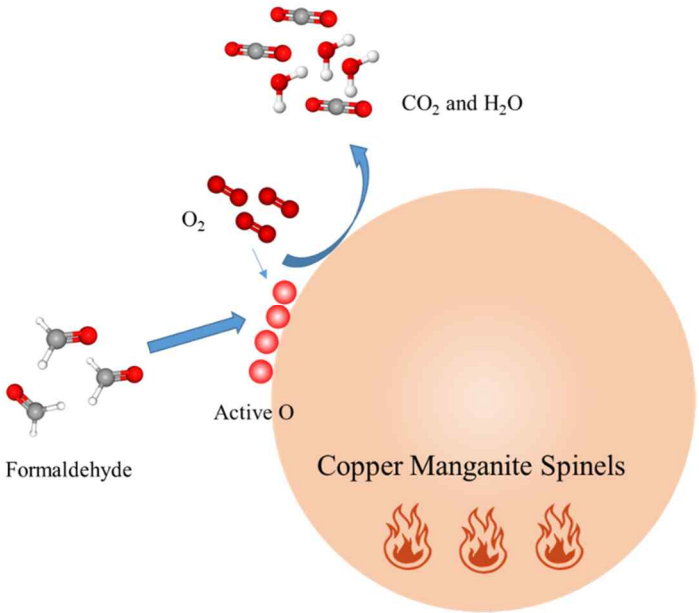

1. Introduction

Indoor air quality control has become a crucial requirement for sustainable health management. The volatile organic compounds (VOCs), particularly formaldehyde (FA), are well-recognized as common indoor air pollutants (Vikrant et al., 2019). Many reports confirmed that contact with FA could lead to severe health issues, including allergic dermatitis, asthma, and even cancers (Ban et al., 2022; Nishikawa et al., 2021). Considering the hazardous nature of FA, the World Health Organization (WHO) proposed many regulations to manage exposure in human subjects (Vellingiri et al., 2020). For instance, the WHO established an indoor air quality guideline for short- and long-term exposures to FA of 0.1 mg m^{-3} (0.08 ppm) (Nielsen et al., 2017). Likewise, the limit of FA concentration in the indoor environment is set to 0.03 mg m^{-3} (~0.02 ppm) by the technical standard for interior pollution control of residential buildings in China (Li et al., 2020).

To date, a plethora of techniques have been proposed to reduce indoor FA levels, including adsorption, plasma catalysis, photocatalytic degradation, and thermocatalytic oxidation (Robert and Nallathambi, 2021). The adsorption method often suffers from the finite adsorption capacity and regeneration of the adsorbent (Bai et al., 2016a). The plasma technique has problems of secondary pollution, high energy consumption, and high cost. The photocatalytic method is limited by the requirement of suitable light sources, and generation of hazardous by-products (Luengas et al., 2015; Zhu et al., 2019). Among the methods mentioned above, thermocatalysis can be regarded as one of the most effective options based on the high VOC removal performance, stability, and capability to continuously oxidize the VOCs into benign end products (e.g., carbon dioxide (CO_2) and water (H_2O)) (Wu et al., 2021).

A list of noble metals (e.g., platinum (Pt), gold (Au), palladium (Pd), rhodium (Rh), and silver (Ag))-

based catalysts have been identified for their thermocatalytic potential against FA at room temperature (RT) (Guo et al., 2019). However, the extensive application of noble metal-based catalysts is limited due to their high costs (Tu et al., 2021). To meet the demand for developing cost-effective materials from a practical perspective, transition metal-based catalysts, particularly manganese-based oxides, have gained much interest in FA thermal degradation due to their good stability, high catalytic activity, abundance, and cost-effectiveness (Wu et al., 2021).

Manganese-based oxides with spinel AB_2O_4 structure have attracted attention for pollutant removal due to their unique structural and physicochemical characteristics (Liu et al., 2016; Yang et al., 2019). The AB_2O_4 spinel structure could be tuned to achieve desirable physicochemical characteristics (e.g., defects, morphology, and electron mobility) with enhanced performance (Zhao et al., 2017). Moreover, the abundant surface oxygen defects and the mobile electron environment caused by the shifting of cations at A and B sites can also enhance oxidation performance (Wang et al., 2017; Wang et al., 2020). Among the transition metal spinels, copper manganite ($CuMn_2O_4$) is a chemically and thermally stable material with unique characteristics of fast electron transfer and variable valences, which are conducive to various catalytic reactions (Zhang et al., 2022; Zhao et al., 2022). Because of these characteristics, $CuMn_2O_4$ has been utilized to remediate various target pollutants such as mercury vapor and nitrogen oxides (Wang et al., 2020; Yang et al., 2019). In addition, the effect of physicochemical properties (e.g., dispersion and microstructure) on the catalytic FA oxidation process of palygorskite-supported copper (Cu) and manganese oxides (MnO_x) have also been studied (Liu et al., 2018). However, there have not been sufficient efforts to adequately evaluate the thermocatalytic performance of pristine $CuMn_2O_4$ against FA under the control of diverse process variables.

In the present study, $CuMn_2O_4$ was synthesized at various Cu/Mn molar ratios (e.g., ¼, ½, and 1) using

a low-temperature sol-gel combustion method to determine the optimum Cu amount for the oxidative removal of FA in the air. Afterward, the catalytic removal performance of optimized $CuMn_2O_4$ was assessed against FA under the control of various process variables (high-temperature pre-treatment environment (hydrogen (H_2) and air), flow rate, catalyst mass, FA concentration, and relative humidity (RH)). The reaction pathway and mechanism were then explored using *in-situ* diffuse reflectance infrared Fourier transform spectroscopy (DRIFTS), density functional theory (DFT) simulations, and temperature-programmed characterizations. The present work offers better support for the construction of transition metal oxides (e.g., $CuMn_2O_4$) for the thermocatalytic oxidative removal of FA under diverse process conditions.

2. Materials and methods

2.1. Chemical reagents

The required materials and chemicals, including Copper(II) nitrate hemi(pentahydrate) ($Cu(NO_3)_2 \cdot 2.5H_2O$; ≥99.99%), manganese(II) nitrate tetrahydrate ($Mn(NO_3)_2 \cdot 4H_2O$; ≥97%), paraformaldehyde (pFA ($HO(CH_2O)_nH$); 95%), and ethanol (CH_3OH; 99.8%) were purchased from Sigma-Aldrich (USA). Citric acid monohydrate ($HOC(COOH)(CH_2COOH)_2 \cdot H_2O$; 99.5%) was supplied by Yakuri Pure Chemicals Co. (Japan). Both air and H_2 (purity of 99.999%) were supplied by Union Gas Co., Ltd. (Yongin, Republic of Korea).

2.2. Catalyst synthesis

The catalysts were prepared using an earlier reported sol-gel combustion method with slight modifications (Wang et al., 2020). Specifically, 0.06 mol of $HOC(COOH)(CH_2COOH)_2 \cdot H_2O$ and 5 mL of

CH_3OH were dissolved in 200 ml of deionized (DI) H_2O with continuous stirring at RT. Subsequently, 0.02 mol of $Cu(NO_3)_2 \cdot 2.5H_2O$ and 0.04 mol of $Mn(NO_3)_2 \cdot 4H_2O$ were dissolved into the solution and stirred at 60°C for 1 h. The solution was placed in a convection oven at 85°C for 24 h to obtain a sticky sol-gel and to dry it thoroughly. The dried powder was calcined in a muffle furnace at 400°C for 4 h to obtain copper manganite spinel materials and further named as $CuMn_2O_4$. For preparing the $Cu_{0.5}Mn_2O_4$ and $Cu_2Mn_2O_4$ catalysts, the amount of $Cu(NO_3)_2 \cdot 2.5H_2O$ utilized in the synthesis was changed to 0.01 and 0.04 mol, respectively, without altering the remaining procedure.

2.3. Characterization instrumentation

The crystalline structures of the prepared catalysts were assessed using powder X-ray diffraction (PXRD) (Bruker Corp., Billerica, MA, USA). The catalyst morphologies, along with their surface elemental compositions, were analyzed with the assistance of a field emission scanning electron microscope equipped with energy dispersive spectrometry (SEM-EDS) (Verios G4UC, Thermo Fisher Scientific Inc., Waltham, MA, USA). Images from a high-resolution transmission electron microscope (HRTEM) model JEM-2100F (JEOL Ltd., Tokyo, Japan) were obtained. The thermal stabilities of the catalysts were evaluated by thermogravimetric analysis (TGA; SDT Q600 AutoDSCQ20 system, TA Instruments, Inc., New Castle, DE, USA). The N_2 adsorption-desorption isotherms were gathered using 3Flex (Micromeritics Instruments Co., USA) for analyzing the Brunauer-Emmet-Teller (BET) surface area and pore size distribution of the catalysts. The surface chemistry of the catalysts was analyzed using X-ray photoelectron spectroscopy (XPS; K-alpha TM system, Thermo Fisher Scientific Co., USA). Charge-correction to adventitious carbon (285 eV) was applied for the collected XPS data (Rudd et al., 2022). The actual bulk Cu and manganese content of the catalysts was analyzed through inductively coupled plasma optical emission spectrometry (ICP-OES)

using the iCAP^{TM} 7000 Series instrument from Thermo Fisher Scientific, Waltham, MA, USA.

The reducibility and desorption features of oxygen species for all prepared catalysts were analyzed by H_2-temperature-programmed reduction (H_2-TPR) and O_2-temperature-programmed desorption (O_2-TPD) systems, respectively (AutoChem II, Micromeritics Instrument Corp., Norcross, GA, USA)) For H_2-TPR experiments, the analysis temperature was raised up to 773.2 K using the heating rates of 5, 10, and 20 K min^{-1}, respectively. The catalyst mass, flow gas, and total volumetric flow rate for these experiments were 50.5 ± 0.3 mg, H_2 (10% in argon (Ar)), and 50 mL min^{-1}, respectively. Isopropyl alcohol was utilized to subcool the outlet of tube (at -80°C) so as to obtain stable signal from thermal conductivity detector (TCD). The above measure was taken to mitigate the impact of formed H_2O while solely measuring the H_2 consumption. Prior to each TPR experiment, loaded catalysts underwent thorough oxidation through exposure it to a 50 mL min^{-1} O_2 flow (5% in Ar). The temperature for these experiments was gradually raised from RT to 383.2 K (10 K min^{-1}) and held for 30 min to eliminate potential interferences such as adsorbed H_2O and/or CO_2. The catalysts underwent cooling to 308.2 K with Ar gas flow (50 mL min^{-1}) for elimination of weakly adsorbed oxygen species.

Prior to each TPD experiment, the loaded catalysts (100.1 ± 0.1 mg) underwent the pretreatment in the temperature range of RT - 383.2 K (heating rate and total molar flow rate of helium (He) as 10 K min^{-1} and 50 mL min^{-1}, respectively). It was maintained at 383.2 K for 30 min to eliminate potential adsorbates such as H_2O and CO_2. Subsequently, the sample underwent cooling to 298.2 K. The sample was saturated by O_2 flow (5% in He) for 30 min. To physically adsorb O_2 molecules, the sample was further treated with a flow rate of 50 mL min^{-1} He gas for 10 min (The TPD analysis commenced at a heating rate of 10 K min^{-1} with a 50 mL min^{-1} He flow, reaching up to 773 K. The detailed data analysis of TPR and TPD is provided in the supplementary information (SI).

154

155 **2.4. FA catalytic oxidation experiments**

156 A fixed-bed quartz tube reactor with an inner radius/length of 2/110 mm was utilized to study the FA
157 catalytic oxidation by Cu-MnO_x catalysts at atmospheric conditions. The catalyst (30-120 mg) and quartz
158 sand (600 mg) were loaded into the quartz reactor and fixed between quartz wool end plugs. The
159 temperature of the catalyst bed was regulated by an electric heater (TC200P, Misung Scientific Co., South
160 Korea). The suffixes "O" and "R" were added to the catalyst names to indicate that the catalyst has
161 undergone oxidation (air) and reduction ($H_2 + N_2$) pre-treatments, respectively at 300°C for 3h with a flow
162 rate of 50 mL min^{-1}.

163 The FA gaseous primary standard (GPS) was prepared by following the standard pFA sublimation
164 method (Yoo et al., 2019). A 5 L (polyester aluminum bag (Top Trading Co., South Korea)) of FA GPS was
165 prepared by the sublimation of pFA powder (100 mg) at 130°C under N_2 flow with a flow rate of 100 mL
166 min^{-1} for 50 min. The quantification of FA GPS was carried out using a standard high-performance liquid
167 chromatography system through the derivatization with 4-dinitrophenylhydrazine (Yoo et al., 2019). To
168 obtain gaseous working standard (GWS) of FA (50-500 ppm), the FA GPS was diluted in a 100 L polyester
169 aluminum bag using pure air. In order to obtain the RH in the range of 30-90% to conduct the catalytic
170 experiments in the co-presence of moisture, 680-2000 μL of DI H_2O was injected into the 100 L FA GWS
171 polyester aluminum bag with the aid of a 500 μL liquid phase syringe (Trajan Scientific and Medical Co.,
172 Australia). The FA flow through the catalyst bed (50-250 mL min^{-1}) was controlled using a mini pump (MP-
173 Σ30N, Sibata Scientific Technology Co., Japan). The catalyst bed temperature was set up from RT (30°C)
174 and raised at 15°C intervals until reaching complete FA conversion (X_{FA}). To ensure a steady state, the
175 temperature at each interval point was sustained for a minimum of 40 min.

The quantification of FA concentration in the reactor effluent was carried out by a gas chromatograph instrument (GC; Shimadzu Model GC-2010, Japan) coupled with a flame ionization detector (FID) and a large volume injection (LVI) unit. The GC-FID conditions (e.g., oven temperature, FID temperature, analysis time, and injection volume) were set at 80°C, 250°C, 4 min, and 1 mL, respectively. In addition, the CO_2 generated by FA oxidation was quantified using a GC-FID equipped with a methanizer system (Shimadzu Model GC-2030, Japan). Note that the methanizer-FID measures carbon oxides (CO_x). The methanizer-FID cannot separately quantify carbon monoxide (CO) and CO_2. However, as excess molecular oxygen (O_2 (21 vol.%)) was used for the oxidation experiments, it was assumed that the CO_x detected by the methanizer-FID was primarily comprised of CO_2. As CO could also be present with CO_2 in the effluent (since CO was detected during FA oxidation in the *in-situ* DRIFTS spectra (see Section 3.5.1)), it should be noted that the detected CO_2 concentration in the effluent by the methanizer-FID was somewhat overestimated.

2.5. Data analysis

The X_{FA} was calculated using Eq. 1. Note that FA_{out} and FA_{in} represent the FA concentration at the outlet and inlet of the fixed bed reactor, respectively. The yield of CO_2 (Y_{CO2}) was estimated by Eq. 2 (Vikrant et al., 2022b). CO_{2t} represents the theoretically expected amount of CO_2 generated through the complete oxidation of FA, while CO_{2e} is the experimentally detected amount of CO_2 at the reactor outlet. In addition, Eq. 3 was utilized to calculate the steady-state reaction rate (r (mmol g^{-1} h^{-1})) (Lee et al., 2021). V_{FA} is the FA GWS flow rate (mol s^{-1}). m_{cat} is the catalyst mass (mg). The determined r value using Eq. 3 is valid exclusively under differential conditions, namely when X_{FA} is less than 20% (Onrubia-Calvo et al., 2022). Hence, the performance comparison was first carried out using the r value derived at X_{FA} = 10%. However,

as the r at lower X_{FA} was difficult to extract from other studies, its value at X_{FA} = 100% has also been calculated and used for simple comparison with other reported catalysts. Under the differential mode of operation, the partial pressures of reactants remain constant across the fixed bed. For simplicity, it was assumed that the disappearance rate of FA ($-r_{FA}$) remains constant irrespective of the position within the fixed bed reactor.

As internal mass transfer limitations can occur during FA oxidation, the Weisz-Prater criterion (C_{WP}) was applied to check whether diffusion in the catalyst pores limits the reaction (Jiménez-Gómez et al., 2021). If the left-hand-side (LHS) term of the C_{WP} is less than the right-hand-side (RHS) value, the internal mass transfer can be neglected. The C_{WP} was applied at the catalyst bed inlet for the harshest test condition (highest FA concentration and temperature). The observed volumetric FA reaction rate ($r^{obs}_{v,FA}$) is the highest at the catalyst bed entrance as the X_{FA} is zero. Hence, if the C_{WP} is satisfied at the reactor inlet, it will be valid for the entire catalyst bed length. As shown in the SI, the C_{WP} was satisfied. Hence, the internal mass transfer limitations can be neglected for all the tested conditions in the present work, i.e., the catalysts operated under the kinetic regime (Jiménez-Gómez et al., 2021).

$$X_{FA}(\%) = \frac{FA_{in} - FA_{out}}{FA_{in}} \times 100 \quad (1)$$

$$Y_{CO_2}(\%) = \frac{CO_{2e}}{CO_{2t}} \times 100 \quad (2)$$

$$\mathrm{r} = \frac{3600 \times 10^6 \times X_{FA} \times V_{FA}}{m_{cat}} \quad (3)$$

2.6. DFT modeling and methodology

The DFT calculations were used to assess the mechanism and energetics of the FA catalytic reaction over the studied catalysts. The Spanish Initiative for Electronic Simulations with Thousands of Atoms

(SIESTA) code has been carried out with a pseudopotential method (Soler et al., 2002). All the calculations were performed employing the Perdew-Burke-Ernzerhof generalized gradient approximation (GGA-PBE) with spin-polarization and +vdW (van der Waals) corrections for precise delineations of weak non-covalent interactions (Dion et al., 2004; Perdew et al., 1996). The atomic positions were effectively optimized during the course of model development based on the DFT simulation. In the optimization course, non-relativistic and norm-conserving pseudopotentials were utilized to describe ion cores. The cut-off radii of Mn, Cu, O, and H was 2.51, 2.08, 1.47, and 1.25 au, respectively (Troullier and Martins, 1991). Furthermore, the expansion of wave functions for all species involved the utilization of a double-ζ plus polarization basis set of localized orbitals f, with the exception of hydrogen, which utilized a double-ζ basis set. The free energies of physical adsorption are defined as $\Delta G = \Delta H + \Delta ST$, where ΔH represents the enthalpy of the physical adsorption calculated by the standard formula $\Delta H = (E_{host + guest} - E_{host} - E_{guests})/N_{guests}$. E represents the total energies of the host before and after the adsorption of guest molecules and the total energy of N guest molecules. The entropy change was calculated by the following formula: $\Delta S = H_{vaporization}/T_{vaporization}$. The values of the enthalpies and temperatures of vaporization were obtained from the National Institute of Standards and Technology (NIST) database. The energy of desorption is the free energy of adsorption with an opposite sign. The energies corresponding with the steps of transformation of FA were defined as the differences between the total energies of products and reactants.

3. Results and discussion

3.1. Physicochemical characterization

The SEM images showed that the $Cu_{0.5}Mn_2O_4$, $CuMn_2O_4$, and $Cu_2Mn_2O_4$ nanoparticles (NPs) were of irregular shapes (Fig. S1(a-c)). The EDS mapping confirmed the presence of Cu, manganese (Mn), and

oxygen in all the synthesized materials (Fig.S1(d-f)). The TEM images further confirmed the irregular shapes of $Cu_{0.5}Mn_2O_4$, $CuMn_2O_4$, and $Cu_2Mn_2O_4$ NPs (Fig. 1). The magnified TEM image of $Cu_{0.5}Mn_2O_4$ indicated the lattice fringe spacing of 0.505 and 0.279 nm, corresponding to the (2 0 0) plane for manganese(IV) oxide (MnO_2) and (2 2 0) plane for $CuMn_2O_4$, respectively (Gao et al., 2021; Tseng et al., 2015) (Fig. 1b). The lattice fringe with an interplanar spacing of 0.488 nm, corresponding to the $CuMn_2O_4$ (1 1 1) plane, was observed for $CuMn_2O_4$ (Wang et al., 2022) (Fig. 1d). The magnified TEM image of $Cu_2Mn_2O_4$ exhibited the lattice fringe spacing of 0.214, 0.257, 0.264, and 0.502 nm, which corresponded with the (4 2 0), (3 1 1), (1 1 1), and (2 0 0) planes of manganese(III) oxide (Mn_2O_3), $CuMn_2O_4$, copper(II) oxide (CuO), and MnO_2, respectively (Li et al., 2015b; Tseng et al., 2015; Wang et al., 2022; Wang et al., 2018b) (Fig. 1f).

The compositional phases of the prepared catalysts were characterized using the PXRD patterns (Fig. 2a). For all the synthesized samples, the primary diffraction peaks at 18.4, 30.3, 35.8, 54.1, 57.6, and 63.4º corresponded with the (1 1 1), (2 2 0), (3 1 1), (4 2 2), (5 1 1), and (4 0 0) lattice planes of $CuMn_2O_4$ (JCPDS 84-0543), respectively, agreeing with the reported literature (Saravanakumar et al., 2017; Zhang et al., 2021). Hence, the successful synthesis of spinel $CuMn_2O_4$ was confirmed in all samples. Interestingly, the diffraction peak at 38.7º detected in all samples should be ascribable to the existence of CuO (JCPDS 89-5895) (Vetrimani et al., 2022). In addition, the peaks at 28.6º and 37.9º indicated the presence of MnO_2 (JCPDS 72-1984) in $Cu_{0.5}Mn_2O_4$ and $Cu_2Mn_2O_4$ (Weina et al., 2017) and Mn_2O_3 (JCPDS 71-0635) in $Cu_2Mn_2O_4$ (Li et al., 2015a), respectively.

$CuMn_2O_4$ displayed high thermal stability, per the TGA data with a minor weight loss (1.1%) from RT to 800°C (Fig. 2b). In contrast, $Cu_{0.5}Mn_2O_4$ and $Cu_2Mn_2O_4$ showed more noticeable mass losses of 1.9 and 3.2%, respectively in the RT-800°C range. Interestingly, both $Cu_{0.5}Mn_2O_4$ and $Cu_2Mn_2O_4$ exhibited similar

TGA profiles with two distinct regions of weight loss including: (i) removal of adsorbed water (RT-460°C) and (ii) phase transformation to MnO_x (> 460°C) (Vikrant et al., 2022b). The larger mass loss of $Cu_2Mn_2O_4$ can be attributed to the phase transformation to MnO_x (e.g., MnO_2 and Mn_2O_3). The superior thermal stability of the catalysts might exert the positive effects (e.g., promoted activation of surface lattice oxygen (O_L)) on the catalytic oxidation of VOCs (Cheng et al., 2022).

The nitrogen (N_2) adsorption-desorption isotherms of $Cu_{0.5}Mn_2O_4$, $CuMn_2O_4$, and $Cu_2Mn_2O_4$ are presented in Fig. 2c. Based on the classification criteria of the International Union of Pure and Applied Chemistry (IUPAC), all the obtained isotherms showed a type-IV pattern with H3-type hysteresis loops (Thommes et al., 2015) (Fig. 2c). In this regard, micropore filling, monolayered, and multilayered N_2 adsorption processes should occur at low, moderate, and high P/P_0 levels, respectively (Vikrant et al., 2022b). The presence of the H3-type hysteresis loop indicates the existence of slit-like pores, likely resulting from aggregated catalyst particles (Sing, 1985). As per the pore size distribution analysis (Fig. 2d), all examined materials predominantly featured mesopores (2-18 nm pore diameter) accompanied by micropores (1-2 nm pore diameter). Among all the tested materials, $CuMn_2O_4$ had the highest BET surface area (21.66 $m^2 g^{-1}$) and pore volume (0.036 $cm^3 g^{-1}$) because of the non-blockage of pores due to the absence of MnO_2 and Mn_2O_3 in its structure (as confirmed by the PXRD results) (Table 1). It is generally believed that high BET surface area and large pore volume can synergistically enhance VOC adsorption for heightened catalytic activity (Liu et al., 2020). The quantified content of Cu and Mn in the prepared catalysts, as determined by ICP-OES, are summarized in Table 1. The experimentally determined Cu and Mn amounts were in good accordance with the theoretical predictions.

The surface chemistry of the tested materials was analyzed using XPS (Fig. S2). The XPS spectrum indicated that all the tested materials contained Cu, Mn, and oxygen in line with the EDS results (Fig. S1).

As illustrated in Fig. S2(a-f), the Cu 2p XPS spectra of all the tested materials could be deconvoluted into four characteristic peaks, Cu $2p_{3/2}$, Cu $2p_{1/2}$, and two satellite peaks (Wang et al., 2019). In this regard, the Cu 2p spectra of all the air pre-treated catalyst materials exhibited two characteristic peaks for Cu^{+} (around 931 and 950.8 eV) and Cu^{2+} (around 933.7 and 953.5 eV) species (Wang et al., 2019) (Fig. S2(a-c)). The characteristic Cu $2p_{3/2}$/Cu$2p_{1/2}$ peaks for $Cu_{0.5}Mn_2O_4$-R, $CuMn_2O_4$-R, and $Cu_2Mn_2O_4$-R were detected at 932.9/952.7, 932.7/952.6, and 932.6/952.5 eV, respectively (Fig. S2(d-f)) (Xu et al., 2019). Hence, metallic Cu (Cu^0), Cu^{+}, and Cu^{2+} species should co-exist in the reduced samples (Wan et al., 2017). $CuMn_2O_4$-O had the highest Cu^{2+} content (72.2%) relative to $Cu_{0.5}Mn_2O_4$ (66.8%) and $Cu_2Mn_2O_4$ (47.9%) (Table 2). The high valence metal states have thus been reported to display better oxidation activity against VOCs (Cheng et al., 2022). The Cu^{2+} content of $Cu_{0.5}Mn_2O_4$-R, $CuMn_2O_4$-R, and $Cu_2Mn_2O_4$-R displayed a 16.3, 29.4, and 16.3% reduction, respectively, relative to their oxidized counterparts, due to the reduction pre-treatment (Table 2).

The Mn 2p XPS spectra for all the analyzed materials were mainly composed of the Mn $2p_{3/2}$ and Mn $2p_{1/2}$ peaks, as presented in Fig. S2(g-l). The Mn $2p_{3/2}$ peak could be deconvoluted into two peaks corresponding with the Mn^{3+} and Mn^{4+} species (Vikrant et al., 2022c). As listed in Table 2, the Mn^{4+} content of the Cu-MnO_x materials increased from 40 to 52.7% with the increment in the Cu content (Cu/Mn ratio from 0.5/2 to 1/2). Hence, increasing the amount of Cu in the Cu-MnO_x materials enhances the Mn^{4+} content (Yi et al., 2018). The high Mn^{4+} content is beneficial for oxidation reactions (Liu et al., 2019). The Mn^{4+} content for $Cu_2Mn_2O_4$-O was estimated as 38.1% (Cu/Mn ratio: 2/2). The Mn^{4+} content for $Cu_{0.5}Mn_2O_4$-R, $CuMn_2O_4$-R, and $Cu_2Mn_2O_4$-R were 31.2, 45.1, and 31.2%, respectively.

The O 1s XPS spectra of the tested materials were shown In Fig. S2(m-r). O 1s spectra of all the tested materials can be deconvoluted into two peaks locating at round 529.6 and 530.9 eV, to match with the O_L

and adsorbed oxygen (O_A) species, respectively (Cheng et al., 2022) (Fig. S2(m-o)). The O_L/O_A peaks for $Cu_{0.5}Mn_2O_4$-O, $CuMn_2O_4$-O, and $Cu_2Mn_2O_4$-O occurred at 529.8/531.0 eV without any shifts. However, the O_L/O_A peaks for $Cu_{0.5}Mn_2O_4$-R, $CuMn_2O_4$-R, and $Cu_2Mn_2O_4$-R displayed slight blue-shifts of +0.2/+0.3, +0.2/+0.2, and +0.1/+0.2 eV, respectively, due to reduction pre-treatment. The relative O_A content of the catalysts decreased in the following order: $CuMn_2O_4$-O (47.2%) > $CuMn_2O_4$-R (44.9%) > $Cu_2Mn_2O_4$-O (43.1%) > $Cu_{0.5}Mn_2O_4$-O (42.4%) > $Cu_{0.5}Mn_2O_4$-R (41.3%) > $Cu_2Mn_2O_4$-R (40.4%). A higher amount of O_A is usually preferable for oxidation reactions (Sun et al., 2019).

3.2. H_2-TPR analysis

Table S1 summarizes the concentration of available surface oxygen for reduction with H_2 in all the tested catalysts. For the A-series of catalysts, the order was $Cu_{0.5}Mn_2O_4$-O (4.98 ± 0.36 $mol_{O*}\ kg_{cat}^{-1}$) < $CuMn_2O_4$-O (7.44 ± 0.40 $mol_{O*}\ kg_{cat}^{-1}$) ≈ $Cu_2Mn_2O_4$-O (7.76 ± 0.33 $mol_{O*}\ kg_{cat}^{-1}$). The available surface oxygen of $CuMn_2O_4$-O seemed to increase by a factor 1.5 when compared to $Cu_{0.5}Mn_2O_4$-O and $Cu_2Mn_2O_4$-O. The above results may be attributed to the fact that a higher amount of available oxygen in Cu-O as $Cu_1Mn_2O_4$-A should contain the highest Cu^{2+}amount (see XPS results). On the other hand, a further increase in the Cu content (compared to $Cu_{0.5}Mn_2O_4$-O and $CuMn_2O_4$-O) does not seem to increase the available oxygen significantly. It can be assumed that the bulk oxygen does not contribute significantly to the reduction reaction.

For the R-series, the relative quantity of the available surface oxygen was in the ascending order of $Cu_{0.5}Mn_2O_4$-R (2.89 ± 0.02 $mol_{O*}\ kg_{cat}^{-1}$) < $CuMn_2O_4$-R (3.56 ± 0.18 $mol_{O*}\ kg_{cat}^{-1}$) < $Cu_2Mn_2O_4$-R (5.50 ± 0.15 $mol_{O*}\ kg_{cat}^{-1}$), which seems to correspond with the increasing Cu loading. Attention must be paid to the fact that all reduction peaks occur at temperatures lower than the prereduction temperature of 573.2 K. The above observation indicates that the oxygen consumed during H_2-TPR comes from the oxidation pretreatment

prior to each H_2-TPR experiment. Higher contents of Cu (x = 0.5 → 1 → 2 in the catalyst $Cu_xMn_2O_4$-R), correspond to higher bulk oxygen. Nonetheless, the reported surface oxygen concentration was not proportional to the molar Cu amounts. Hence, for the $Cu_{0.5}Mn_2O_4$-R catalyst, a greater reduction can be expected during the reduction pretreatment than those with higher Cu contents. The above result corresponds to a higher oxygen vacancy (OV) concentration, which can be replenished during pretreatment.

Using Eq. (S5) for the TPR data modeling, 9 or 12 parameters were employed for modeling the experimental data. The above corresponds to 3 or 4 peaks within each profile and three parameters are dedicated to each peak. A negligible scaling factor was obtained in the Gaussian profile when employing four peaks for data modeling. Therefore, three peaks were used to describe the data (Fig. S3-S5). The above statistically corresponds to the fact that the peak needs to be removed from the model as it does not significantly contribute to describing the experimental data. The holistic modeling of TPR data with Eq. (S5) yielded a maximum average error (e_{max}) of 1.41 % (observed over $Cu_2Mn_2O_4$-R at 20 K min^{-1}) when comparing the average error in relation to the maximum signal per TPR experiment (Eq. (4)). S was determined with Eq. (S6). With the formula, n and y_{max} denote the data point number and the maximal output value (a.u.) for each experiment, respectively.

$$e_{max} = \frac{1}{y_{max}} \cdot \sqrt{\frac{S}{n}} \quad (4)$$

Table S2-4 lists the kinetic parameters derived for the $Cu_{0.5}Mn_2O_4$-O, $CuMn_2O_4$-O, and $Cu_2Mn_2O_4$-O reduction, respectively. In Table S2, peaks 1, 2, and 3 accounted for 10.0 ± 0.4, 78.2 ± 0.1, and 11.8 ± 1.1% of the overall signal, respectively. In Table S3, peaks 1, 2, 3, and 4 accounted for 7.1 ± 1.2, 59.4 ± 3.6, 33.5 ± 8, and 18 ± 4.3% of the overall signal, respectively. In Table S4, peaks 1, 2, and 3 accounted for 28.2 ± 2.2, 41.4 ± 0.5, and 30.4 ± 3.6% of the total signal, respectively. Fig. S3 (a, b, c), Fig. S4 (a, b, c), and Fig. S5 (a, b, c)

gives the experimental H_2-TPR profiles and Gaussian model profiles for the $Cu_{0.5}Mn_2O_4$-O, $CuMn_2O_4$-O, and $Cu_2Mn_2O_4$-O catalysts at the heating rates of 5-20 K min^{-1}, respectively. An effective fit was noticeable, and each individual peak Gaussian profile can be defined by parameters $(a, \mu, \sigma)_{i=1\ldots4.}$ (Note that these results are not displayed.) The regression analysis of the pairs (T_{max}, β), according to Eq. (S15), delivers the activation energy E_i and pre-exponential factor A_i for each reduction peak: see Tables S2 to S4. The results are presented in Figure S6.

The activation energy values (in kJ mol^{-1}) over $Cu_{0.5}Mn_2O_4$-O are estimated in the order of 62.9 ± 3.6 (peak 1) < 76.7 ± 4.7 (peak 2) < 110.1 ± 24.1 (peak 3): see Table S2. The initial peak, observed at lower reduction temperatures, seems to exhibit the lowest activation energy. The activation energy values (in kJ mol^{-1}) for the reduction of H_2 over $CuMn_2O_4$-O was 87.1 ± 0.2 (peak 1) ≈ 88.4 ± 0.9 (peak 4) < 135.9 ± 4.6 (peak 3) < 158.6 ± 2.3 (peak 4): see Table S3. The reduction coefficients (in s^{-1}) at the corresponding T_{max} for β = 10 K min^{-1} are in the order of 0.0863 (peak 1) > 0.0127 (peak 2) > 0.0097 (peak 3) > 0.0061 (peak 4). The activation energy for the reduction of H_2 over $Cu_2Mn_2O_4$-O can be in the order of 48.3 ± 6.8 (peak 1) < 56.8 ± 1.8 (peak 2) < 64.1 ± 11.2 (peak 3) kJ mol^{-1}, see Table S4. Table S5-S7 listed the obtained kinetic parameters for the reduction of the $Cu_{0.5}Mn_2O_4$-R, $CuMn_2O_4$-R, and $Cu_2Mn_2O_4$-R, respectively. Peaks 1, 2, 3, and 4 accounted for 13.2 ± 1.1, 9.1 ± 1.5, 77.7 ± 2.6, and 34.6 ± 2.2% of the total signal for $Cu_{0.5}Mn_2O_4$-R, respectively (Table S5). Peaks 1, 2, and 3 accounted for 14.0 ± 0.5, 69.2 ± 0.2, and 16.8 ± 2.3% of the total signal for $CuMn_2O_4$-R, respectively (Table S6). In Table S7, peaks 1, 2, 3, and 4 accounted for 20.4 ± 1.0, 18.8 ± 5.7, 60.8 ± 10.5, and 12.6 ± 2.7% of the overall signal for $Cu_2Mn_2O_4$-R, respectively.

Figure. S3 (d, e, f), Figures S4 (d, e, f), and S5 (d, e, f) give the experimental H_2-TPR profiles and Gaussian model profiles for the $Cu_{0.5}Mn_2O_4$-R, $CuMn_2O_4$-R, and $Cu_2Mn_2O_4$-R catalysts at the heating rates of 5-20 K min^{-1}, respectively. An effective fit was noticeable, and each individual peak Gaussian profile can

be defined by parameters $(a, \mu, \sigma)_{i=1\ldots4.}$ (Note that these results are not displayed.) The regression analysis of the pairs (T_{max}, β), according to Eq. (S15), delivers the activation energy E_i and pre-exponential factor A_i for each reduction peak: see Tables S5 to S7. The results are presented in Figure S6. The activation energy values (in kJ mol^{-1}) over $Cu_{0.5}Mn_2O_4$-R can be ordered according to 61.3 ± 7.4 (peak 3) < 81.6 ± 5.0 (peak 4) < 108.0 ± 5.6 (peak 1) < 126.6 ± 0.8 (peak 2): see Table S5. The initial peak, observed at lower reduction temperatures, seems to exhibit the lowest activation energy. However, the corresponding pre-exponential factors of peaks 1 and 2 were six orders of magnitude more significant than those of peak 3 and 4 values, respectively. Furthermore, when evaluating the reduction coefficients (in s^{-1}) at the corresponding T_{max} for β = 10 K min^{-1}, the order was as follows: 0.0134 (peak 1) > 0.0118 (peak 2) > 0.0071 (peak 3) ≈ 0.0083 (peak 4).

The activation energy values (in kJ mol^{-1}) for H_2 reduction over $CuMn_2O_4$-R are estimated in the order of 96.0 ± 7.6 (peak 3) < 107.7 ± 10.4 (peak 2) < 130.4 ± 11.5 (peak 1): see Table S6. The above order seems to be the reverse order of the corresponding reduction temperature. The evaluation of the reduction coefficients (in s^{-1}) at the corresponding T_{max} for β = 10 K min^{-1} shows the order of 0.0166 (peak 1) > 0.0104 (peak 2) > 0.0091 (peak 3). The activation energy values (in kJ mol^{-1}) for the reduction of H_2 over $Cu_2Mn_2O_4$-R can be placed in the order of 94.1 ± 9.1 (peak 4) ≈ 99.1 ± 6.8 (peak 3) < 124.7 ± 27.7 (peak 1) ≈ 127.5 ± 31.1 (peak 2): see Table S7. The initial peak, observed at lower reduction temperatures, seems to exhibit the lowest activation energy. However, the corresponding pre-exponential factors of peaks 1 and 2 were 3 to 4 orders of magnitude more significant than those of the peaks 3 and 4 values, respectively. The reduction coefficients (in s^{-1}) at the corresponding T_{max} for β = 10 K min^{-1} are estimated in the order 0.0170 (peak 1) ≈ 0.0163 (peak 2) > 0.0097 (peak 3) ≈ 0.0095 peak (4). The reduction coefficient was determined through the application of the activated complex theory (Eyring, 1935), as depicted in Eq. (5). The activation entropy ($\Delta S^{\neq}$) can be computed based on the pre-exponential factor, A, as shown in Eq. (6).

$$k = A \cdot \exp\left(-\frac{E}{RT}\right) = \exp\left(-\frac{\Delta G^{\neq}}{RT}\right) = \exp\left(\frac{\Delta S^{\neq}}{R}\right) \cdot \frac{kT}{h} \cdot \exp\left(-\frac{\Delta H^{\neq}}{RT}\right) \quad (5)$$

$$\Delta S^{\neq} = R \cdot \ln\left(\frac{hA}{kT}\right) \quad (6)$$

$\Delta S^{\neq}$ signifies the disparity in entropy between the reactants (H_2 and O*) and the activated complex (yielding H_2O and a reduced surface). According to thermodynamic equation ($\Delta G^{\neq} = \Delta H^{\neq} - T \cdot \Delta S^{\neq}$), the significance of $\Delta S^{\neq}$ lies in its contribution to the equilibrium shift between the reactants and activated complexes. The surface reduction reaction would likely shift the equilibrium to favorably form the activated complex, as the elevation of $\Delta S^{\neq}$ results in a reduction of $\Delta G^{\neq}$ (Vyazovkin, 2021). In addition, the positive $\Delta S^{\neq}$ values indicate increasing entropy as the system approaches the transition state. The above relationship signifies a dissociative mechanism, with the activated complex loosely bound and ready for dissociation. Negative values suggest that the entropy decreases during the formation of the transition state. The decrease in entropy often corresponds to an associative mechanism in which two reaction partners form a single activated complex (Espenson, 1995).

Inspection of the $\Delta S^{\neq}$ values shows that on the $CuMn_2O_4$-O catalyst, a positive value (34.8 ± 3.5 J mol^{-1} K^{-1}) was obtained. The other values for the A-series were all negative. The above observation might be the reason that the $CuMn_2O_4$-O catalyst is the most active, i.e., the activated complex for H_2O formation exhibits loose binding and is prone to leave the surface rather than stay in the case of an associative mechanism. For the R-series, positive $\Delta S^{\neq}$ values were found for $Cu_{0.5}Mn_2O_4$-R (peak 2), $CuMn_2O_4$-R (peak 1), and $Cu_2Mn_2O_4$-R (peak 1 and 2). The 33.3 ± 4.4 J mol^{-1} K^{-1} of the $CuMn_2O_4$-R catalyst was similar to that for the $CuMn_2O_4$-O catalyst. However, the available surface oxygen of $CuMn_2O_4$-O was ~2.6 times higher than that of $CuMn_2O_4$-R (Table S1), indicating its superior catalytic activity.

3.3. O_2-TPD analysis

The O_2-TPD analysis for all tested catalysts is displayed in Figure S7. For all $Cu_{0.5}Mn_2O_4$ and $CuMn_2O_4$ catalysts, 4 peaks were utilized to describe the desorption process of O_2. A satisfactory fitting of the calculated signal was observed with an e_{max} of less than 2.79% (Table S8 and S9). For the $Cu_2Mn_2O_4$ catalysts, 5 peaks (with all significant parameters) are used to describe the experimental data with a e_{max} of 4.93% (observed over $Cu_2Mn_2O_4$-O catalyst as listed in Table S8). The $CuMn_2O_4$-O catalyst displayed the highest O_2 adsorption of 120.5 ± 3.4 $mmol_{O2}$ kg_{cat}^{-1} of all A-series catalysts. The desorption coefficient values at 90°C (temperature of 90% X_{FA}) for the catalysts $Cu_xMn_2O_4$-O, x = 0.5, 1, and 2 were derived as 0.0164, 0.0075, and 0.0062 s^{-1}, respectively. Because the O_2 adsorbate concentration ratio between $CuMn_2O_4$-O and $Cu_{0.5}Mn_2O_4$-O (or $Cu_2Mn_2O_4$-O) was ~2.9, the superior activity of the $CuMn_2O_4$-O was once more demonstrated using the TPD experiments.

$Cu_{0.5}Mn_2O_4$-R and $CuMn_2O_4$-R catalysts exhibited similar results in signal contribution, activation energy values, and pre-exponential factors for O_2 desorption (Table S9). For example, the four peak contribution signal values for $Cu_{0.5}Mn_2O_4$-R were 9.8, 10.4, 38.4, and 41.1%, respectively. For the $CuMn_2O_4$-R catalyst, the four peak contribution signal values were 7.9, 11.2, 40.4, and 40.5%, respectively. The primary difference was in the O_2 adsorbate concentrations with 105.4 ± 3.0 and 73.8 ± 2.4 $mmol_{O2}$ kg_{cat}^{-1}, respectively. Catalyst $Cu_2Mn_2O_4$-R shows a lower adsorbate concentration of 48.7 ± 1.6 $mmol_{O2}$ kg_{cat}^{-1}, while peaks 4 and 5 amount to 59.4 % of the total signal. The peak with the highest temperature, representing the most challenging adsorbates to remove through desorption, contributed to ~ 41% of the total signal for $Cu_{0.5}Mn_2O_4$-R and $CuMn_2O_4$-R catalysts. The above observation suggests that under the inert conditions of O_2-TPD, bulk oxygen (rather than O_2 surface adsorbates) escapes to corroborate the earlier conclusions.

3.4. Catalytic FA removal performance

As shown in Fig. 3a, the catalytic efficiency of the studied catalysts against FA (per their light-off curves) decreased in the following order: $CuMn_2O_4$-O > $CuMn_2O_4$-R > $Cu_{0.5}Mn_2O_4$-O > $Cu_2Mn_2O_4$-O > $Cu_{0.5}Mn_2O_4$-R > $Cu_2Mn_2O_4$-R. The T_{90} (temperature at 90% X_{FA}) values for 50 ppm FA increased as follows: $CuMn_2O_4$-O (85°C) < $CuMn_2O_4$-R (93°C) < $Cu_{0.5}Mn_2O_4$-O (100°C) < $Cu_2Mn_2O_4$-O (102°C) < $Cu_{0.5}Mn_2O_4$-R (103°C) < $Cu_2Mn_2O_4$-R (108°C) (Table 3). The above findings indicate consistently that the FA removal performance should increase with the corresponding rise in the Cu content (Cu/Mn ratio from 0.5/2 to 1/2). However, a further increase in the Cu content (Cu/Mn ratio: 2/2) lowered the FA removal performance due to the agglomeration of catalyst particles. Also, the oxidized catalysts outperformed their reduced counterparts. These observations might be attributed to the high content of oxidized metal species (e.g., Cu^{2+}) and O_A (see Section 3.1). As such, the highest catalytic performance for the $CuMn_2O_4$-O, followed by $CuMn_2O_4$-R, was observed for FA oxidative removal. Furthermore, the r value at the maximal removal efficiency of prepared catalysts were compared to assess the catalytic performance of $CuMn_2O_4$-A in relation to other catalyst forms (Table 3). Accordingly, their performances are found in the order of $CuMn_2O_4$-O (4.19E-02 mmol g^{-1} h^{-1} (X_{FA}= 100%)) > $CuMn_2O_4$-R (3.65E-02 mmol g^{-1} h^{-1} (X_{FA}= 87%)) > $Cu_{0.5}Mn_2O_4$-O (2.77E-02 mmol g^{-1} h^{-1} (X_{FA}= 66%)) > $Cu_2Mn_2O_4$-O (2.43E-02 mmol g^{-1} h^{-1} (X_{FA}= 58%)) > $Cu_{0.5}Mn_2O_4$-R (2.39E-02 mmol g^{-1} h^{-1} (X_{FA}= 57%)) > $Cu_2Mn_2O_4$-R (1.93E-02 mmol g^{-1} h^{-1} (X_{FA}= 46%)). The best-performing catalyst, $CuMn_2O_4$-O, was thus chosen to study the impact of process variables on FA catalytic removal efficiency in subsequent experiments.

Firstly, the effects of the catalyst mass on the FA removal performance were studied using $CuMn_2O_4$-O at 90°C. Accordingly, the X_{FA} decreased with reduced m_{cat} in the order of 120 mg (100%) > 60 mg (32%) > 30 mg (15%) (Fig. 3b). The FA removal performance is reduced at low m_{cat} due to a decrease in the number

of active surface sites (Vikrant et al., 2022b; Vikrant et al., 2023). As displayed in Fig. 3c, the X_{FA} performance of $CuMn_2O_4$-O at 90°C, when measured across increasing FA concentrations (50 to 500 ppm), exhibited a declining trend: 100% (50 ppm) > 43% (250 ppm) > 29% (500 ppm). The active surface sites might likely be saturated at increased FA concentration to decrease the X_{FA} (Etim et al., 2019).

Moreover, when the feed flow rate increased from 50 ml min^{-1} (gas hourly space velocity (GHSV): 3,979 h^{-1}) to 250 ml min^{-1} (GHSV: 19,895 h^{-1}), the efficiency of FA removal exhibited a decrease for $CuMn_2O_4$-A catalyst. The X_{FA} at 90°C decreased in the following order: 50 ml min^{-1} (100%) > 100 ml min^{-1} (61%) > 250 ml min^{-1} (32%) (Fig. 3d). Decreasing the contact time between FA molecules and catalyst in the reactor at elevated flow rates should have lowered X_{FA} (Etim et al., 2019). The increase in RH level caused the catalytic efficiency (X_{FA} (at 90°C)) of $CuMn_2O_4$-O to decrease in the order of 100% (RH0%) > 65% (RH 30%) () > 61% (RH60%) > 51% (RH90%) (Fig. 3e). The anticipated decrease in FA removal performance in the presence of moisture was due to the competition between FA and H_2O molecules for the same active surface sites (Etim et al., 2019; Vikrant et al., 2022b). The durability of the catalyst was studied by a conducting time-on-stream (TOS) test at optimal temperature (90°C) and RT, respectively (Fig. 3f and Fig. S8). The steady-state RT X_{FA} for $CuMn_2O_4$-O was maintained at ~ 25% with Y_{CO2} of ~ 10% for at least 240 min (4 h) (Fig. S8). In contrast, stable maintenance of 100% X_{FA} to CO_2 was obtained for at least 12 h TOS at 90°C (Fig. 3f). Such observations indicate that higher temperatures were favorable for the catalytic oxidation of FA. Moreover, no significant deactivation was observed in the TOS experiments (Fig. 3f and Fig. S8). These findings may thus indicate the high durability of $CuMn_2O_4$-O for the practical air purification applications.

3.5. FA oxidation pathway and mechanism

3.5.1. *In-situ* DRIFTS

In-situ DRIFTS analysis was conducted in the presence (Fig. 4) and absence (Fig. S9) of O_2 to assess the FA oxidation pathway for $CuMn_2O_4$-O, the best-performing catalyst. In the presence of O_2, the following species were identified on the $CuMn_2O_4$-O surface through the FA oxidation reaction (Fig. 4): (i) molecularly adsorbed FA (954 cm^{-1}), (ii) dioxymethylene (DOM: $\delta(CH_2)$/ $\upsilon(CO)$ (1126 cm^{-1}/ 1442 cm^{-1}) (Fig. S10a)), (iii) formate ($HCOO^-$: $\upsilon_s(OCO)$/ $\upsilon_{as}(OCO)$ (1354 and 1582 cm^{-1}) and $\upsilon(CH)$ (2867 and 2933 cm^{-1}) (Fig. S10b)), (iv) CO (1879-2028 cm^{-1}), (v) surface hydroxyl (OH) and H_2O (3493-3973 cm^{-1}), and (vi) CO_2 (2336 cm^{-1}) (Chen et al., 2020; Liu et al., 2018; Vikrant et al., 2022a). Accordingly, the initial adsorption of FA molecules occurred on the active surface sites and then reacted with activated surface oxygen molecules (O*) to produce CO_2 and H_2O as the final product through DOM, $HCOO^-$, and CO intermediates. The intensity of the CO_2 band at 2336 cm^{-1} decreased slightly with time, likely due to its desorption from the catalyst surface. Interestingly, identical reaction intermediates mentioned earlier were also recorded in the *in-situ* DRIFTS spectrum obtained under the O_2 deficient condition (N_2 environment) (Fig. S8). These observations suggest that surface O* should be the primary oxidant in the FA catalytic oxidation process on the surface of $CuMn_2O_4$-O (Vikrant et al., 2023).

The adsorbed FA molecules react with O* on the catalyst surface to form DOM species (Sun et al., 2018). The DOM species combine with O* for the formation of $HCOO^-$ (Chen et al., 2020). Then, $HCOO^-$ species decompose into H_2O and CO molecules. Subsequently, the CO species react with O* to form CO_2 (Vikrant et al., 2022a; Zhang et al., 2006). In addition, $HCOO^-$ could also be converted directly into CO_2 and H_2O by reacting with the surface OH groups (Bai and Li, 2014; Li et al., 2018). The negative absorbance bands for the surface OH species indicate consumption during the catalytic oxidation of FA to support the

direct dissociation of the $HCOO^-$ species. The H_2O produced from FA oxidation could also supply the surface OH groups to sustain the $HCOO^-$ dissociation pathway. The absence of adsorbed H_2O peak was attributed to its rapid conversion into surface OH (Fig. 4 and Fig. S9) (Vikrant et al., 2022b). In contrast, the H_2O supplied by the moisture can lower the overall FA removal performance of $CuMn_2O_4$-O (see Section 3.4) by competing for the active surface sites. The O* consumed for FA oxidation may form OVs, while being replenished through O_2 dissociation (Liu et al., 2016). It can also be inferred that O_L and O_A species in the $CuMn_2O_4$-O could exist in the active state (O*) to induce the FA oxidation process as FA oxidation can proceed in the absence of O_2. Interestingly, the peaks of molecularly adsorbed FA and $HCOO^-$ at band of 954 and 1354 or 1582 cm^{-1} in the air atmosphere were weaker than that of in the N_2 environment (Fig. 4 and Fig. S9). This observation may imply the less accumulation of FA and $HCOO^-$ species over the surface catalysts in the air environment compared to that in the N_2 environment (Zhu et al., 2017). Also, this indicated these species may transform or desorb faster at the former condition (e.g., air environment) (Zhu et al., 2017). FA oxidation without air (e.g., N_2 environment) cannot be maintained for extended periods as the replenishment of OVs through O* consumption is confined (Vikrant et al., 2022a).

3.5.2. DFT simulation

The FA oxidation pathways over the $CuMn_2O_4$ substrate were studied with the aid of a series of first principle calculations. A slab of 224 atoms constructed from the 2×2×2 supercell was used to assess the FA oxidation pathway over the $CuMn_2O_4$ substrate (Fig. S11). At the first step of the simulation, three initial configurations of FA and O_2 on the surface of the substrate were checked. The first configuration corresponded with the physical adsorption of FA and O_2 on manganese and Cu, respectively (Fig. 5 (a)). The second configuration involved the adsorption of both molecules on the nearest manganese atoms on

526 the substrate surface (Fig. 5 (f)). The third configuration corresponded with the physical adsorption of FA
527 and O_2 on Cu and manganese, respectively (Fig. 5). The third configuration was less favorable (about 20
528 kJ mol^{-1}) than the former. The calculated free energies of adsorption indicated stable adsorption at RT.
529 Further, temperature increases turned adsorption from stable to metastable due to increasing contribution
530 from the entropy. In the case of the third configuration, adsorption turned from metastable to unstable even
531 at 50ºC.

532 The subsequent stage of the catalytic oxidation process for FA involved the transition of a hydrogen
533 atom from FA to O_2 with the formation of —OCH and —OOH groups on the surface (Fig. 5 (b) and (g)).
534 Note that transforming O_2 to —OOH groups excludes energetically unfavorable activation of O_2. The above
535 step was endothermic for both the studied pathways (+200.1 and +128.0 kJ mol^{-1} for the first and second
536 configurations, respectively). However, the above-described second pathway required almost two times
537 less energy than the first pathway (128 versus 200 kJ mol^{-1}). The second step of the catalytic reaction was
538 OH group migration from —OOH to the —OCH group with the formation of the —OCHOH group on the
539 surface (Fig. 5 (c) and (h)). The third step was hydrogen migration from the —OCHOH group with the
540 formation of OH and —OCHO groups on the surface (Fig. 5 (d) and (i)). The final step of the reaction was
541 the hydrogen transfer from —OCHO to the OH group, with the formation of H_2O and CO_2 molecules
542 physically adsorbed on the surface (Fig. 5 (e) and (j)). For both pathways, the second and subsequent steps
543 were exothermic. Note that the energy magnitudes of some steps in each pathway overcome the energy
544 expenditure magnitude for the first step. Therefore, the conversion of the first FA molecule will supply the
545 energy needed to convert an increasing number of the following FA molecules.

546 The last step of the modeling was the calculation of the energies required for desorption. For the
547 configuration shown in Fig. 5 (e), the Gibbs free energy of desorption was -2.9 kJ mol^{-1} at RT. For another

548 configuration (Fig. 5 (i)), desorption of the molecules from the surface at RT was an endothermic process
549 with an energy cost of 23.1 kJ mol^{-1}. Increasing the temperature enhanced the contribution from the entropy,
550 leading to a decrease in the energy cost of the desorption. Note that the energy cost of removing the reaction
551 products, including H_2O, agrees with the experimentally observed activity decay at lower temperatures with
552 increasing moisture. Thus, the calculations demonstrate two possible pathways for the oxidation of FA to
553 CO_2. The most efficient pathway shown in Figs. 5 (f)-(i) involves only the manganese atoms on the surface.
554 The above result explains the experimental data wherein the FA oxidation activity insignificantly depends
555 on the Cu content. The calculated energy cost of the first step of the reaction agreed with the significant
556 increment in the FA oxidation activity with rising temperature, as observed experimentally.
557

558 **3.6. FA oxidation performance comparison**

559 To gain more insights into the viability of our catalytic system, the catalytic oxidation performance of
560 the $CuMn_2O_4$ catalysts against FA was assessed in comparison to other catalysts reported in the literature
561 in terms of the r value at 10% X_{FA} and 90°C (Table 4). The use of r for such evaluation has been
562 recommended as its derivation involves the incorporation of the key process variables and parameters (e.g.,
563 V_{FA}, m_{cat}, and FA concentration) into a single quantitative value (Guo et al., 2021; Vikrant et al., 2021). As
564 summarized in Table 4, the Ag-cerium(IV) oxide (CeO_2) was found as the best performer when assessed in
565 terms of the reaction kinetic rate (r (at 10% X_{FA}) = 3.66E-01 mmol g^{-1} h^{-1} at 50°C) followed by the three-
566 dimensional (3D)-manganese oxide (MnO_2) (4.39E-02 mmol g^{-1} h^{-1} at 60°C), two-dimensional (2D)-
567 cobalt(II,III) oxide (Co_3O_4) (3.92E-02 mmol g^{-1} h^{-1} at 100°C), β-MnO_2 (3.67E-02 mmol g^{-1} h^{-1} at 125°C),
568 and nano-cobalt(II,III) oxide (Co_3O_4) (3.19E-02 mmol g^{-1} h^{-1} at 185°C) (Bai et al., 2013; Bai et al., 2016b;
569 Ma et al., 2014). The superior performance of Ag-CeO_2 should be attributed to the abundance of surface

570 O_A species and the interaction between Ag and CeO_2 (Ma et al., 2014).

571 The performance comparison was further conducted in terms of their r value at 100% X_{FA} at 90°C as
572 it is difficult to estimate the r value at 10% X_{FA} from most of the reported catalytic systems. (Note that the
573 r values derived at X_{FA} > 20% may overestimate the actual performance (Onrubia-Calvo et al., 2022).)
574 According to this expanded performance comparison, the top five thermocatalysts (i.e., in terms of the r
575 value at 100% X_{FA} at 90°C) for the FA oxidative removal are recognized as Ag-cerium(IV) oxide (CeO_2)
576 (1.50 mmol g^{-1} h^{-1}) > Ag-0.9%-potassium (K)/MnO_2 (3.62E-01 mmol g^{-1} h^{-1}) > three-dimensional (3D)-
577 manganese oxide (MnO_2) (1.53E-01 mmol g^{-1} h^{-1}) > Ag-1.5%-MnO_2-Eggshell (8.05E-02 mmol g^{-1} h^{-1}) >
578 $CuMn_2O_4$-O (4.19E-02 mmol g^{-1} h^{-1})(Bai et al., 2016b; Lu et al., 2018; Ma et al., 2014; Vikrant et al.,
579 2022b).

580 The superior performance of Ag-CeO_2 was attributed to the abundance of surface O_A species and the
581 Ag-CeO_2 synergy (Ma et al., 2014). Despite the excellent FA oxidation performance of all the supported
582 Ag catalysts, their practical application is largely restricted due to the high cost of the noble metal used (Lu
583 et al., 2018; Ma et al., 2014; Vikrant et al., 2022b). Moreover, according to a survey of data provided in
584 Table 4, other catalysts (such as $Mn_{0.5}Ce_{0.5}O_2$ (r: 1.33E-02 mmol g^{-1} h^{-1}), CeO_2 (r: 4.02E-03 mmol g^{-1} h^{-1}),
585 and β-MnO_2 (r: 4.02E-03 mmol g^{-1} h^{-1})) show relatively inferior FA oxidation performances than $CuMn_2O_4$-
586 O (r: 4.19E-02 mmol g^{-1} h^{-1}) (Bai et al., 2016b; Huang et al., 2016; Li et al., 2014). As such, the $CuMn_2O_4$-
587 A catalyst used in the present work is found as a better alternative in terms of cost economics and good
588 catalytic performance for practical low-temperature FA oxidation applications.

589

590 **4. Conclusions**

591 In the present research, the oxidative removal of FA at low temperatures in the air was studied by

$CuMn_2O_4$ catalysts. X_{FA} at 90°C at a GHSV of 3,979 h^{-1} (50 ppm FA) for the tested catalysts decreased in the following order: $CuMn_2O_4$-O (100%) > $CuMn_2O_4$-R (87%) > $Cu_{0.5}Mn_2O_4$-O (66%) > $Cu_{0.5}Mn_2O_4$-R (57%) > $Cu_2Mn_2O_4$-O (53%) > $Cu_2Mn_2O_4$-R (46%). A moderate Cu/Mn ratio (1/2) and air pretreatment significantly enhanced the catalytic performance of the catalysts. As such, $CuMn_2O_4$-O was identified as the best-performing catalyst due to large amounts of O_A and oxidized metal species (e.g., Cu^{2+} and Mn^{4+}) on its surface. $CuMn_2O_4$-O was also used to assess its FA oxidation performance as a function of various process variables, such as FA concentration, m_{cat}, flow rate, and RH level. *In-situ* DRIFTS indicated DOM, $HCOO^-$, and CO as the primary FA oxidation reaction intermediates. DFT simulations and calculations were in line with experimental observations. According to the performance comparison, the $CuMn_2O_4$-O can be regarded as a good alternative for low-temperature oxidative removal of FA due to its cost economics (no noble metals) and good catalytic activity (r=4.19E-02 mmol g^{-1} h^{-1}). The present work is expected to provide the necessary insight into applying $CuMn_2O_4$ transition metal oxide catalysts for the low-temperature oxidative removal of FA in the air. Future studies should focus upon the design of high-performance transition metal oxide catalysts (e.g., doping ultra-low noble metal content) for the RT oxidative removal of FA without the requirement of external energy (e.g., heat).

Acknowledgments

This work was supported by a grant from the National Research Foundation of Korea (NRF) funded

by the Ministry of Science and ICT (MSIT) of the Korean government (Grant No: 2021R1A3B1068304). P.M.H. would like to thank the Research and Development Program of Ghent University Global Campus (GUGC), Korea. This research was also supported by Korea Basic Science Institute (National Research Facilities and Equipment Center) grant funded by the Ministry of Education (2022R1A6C101A779).

References

Bai, B., et al., 2013. Comparison of the performance for oxidation of formaldehyde on nano-Co3O4, 2D-Co3O4, and 3D-Co3O4 catalysts. Applied Catalysis B: Environmental. 142, 677-683.

Bai, B., Li, J., 2014. Positive effects of K^+ ions on three-dimensional mesoporous Ag/Co_3O_4 catalyst for HCHO oxidation. Acs Catalysis. 4, 2753-2762.

Bai, B., et al., 2016a. Progress in research on catalysts for catalytic oxidation of formaldehyde. Chinese Journal of Catalysis. 37, 102-122.

Bai, B., et al., 2016b. Synthesis of three-dimensional ordered mesoporous MnO2 and its catalytic performance in formaldehyde oxidation. Chinese Journal of Catalysis. 37, 27-31.

Ban, J., et al., 2022. Ambient formaldehyde and mortality: A time series analysis in China. Science Advances. 8, eabm4097.

Chen, X., et al., 2020. Identification of a facile pathway for dioxymethylene conversion to formate catalyzed by surface hydroxyl on TiO_2-based catalyst. ACS Catalysis. 10, 9706-9715.

Cheng, Q., et al., 2022. A novel $Cu_{1.5}Mn_{1.5}O_4$ photothermal catalyst with boosted surface lattice oxygen activation for efficiently photothermal mineralization of toluene. Nano Research. 1-9.

Dion, M., et al., 2004. Van der Waals density functional for general geometries. Physical review letters. 92, 246401.

Espenson, J. H., 1995. Chemical kinetics and reaction mechanisms. Citeseer.

Etim, U. J., et al., 2019. 3. Functional catalysts for catalytic remova l of formaldehyde from air. Environmental Functional Nanomaterials, De Gruyter2020. 89-126.

Eyring, H., 1935. The activated complex in chemical reactions. The Journal of Chemical Physics. 3, 107-115.

Gao, Y., et al., 2021. CuMn2O4 spinel nanoflakes for amperometric detection of hydrogen peroxide. ACS Applied Nano Materials. 4, 6832-6843.

Guo, J., et al., 2019. Review on noble metal-based catalysts for formaldehyde oxidation at room temperature. Applied Surface Science. 475, 237-255.

Guo, Y., et al., 2021. Recent advances in VOC elimination by catalytic oxidation technology onto various nanoparticles catalysts: a critical review. Applied Catalysis B: Environmental. 281, 119447.

Huang, Y., et al., 2016. Bifunctional catalytic material: an ultrastable and high-performance surface defect CeO_2 nanosheets for formaldehyde thermal oxidation and photocatalytic oxidation. Applied Catalysis B: Environmental. 181, 779-787.

Jiménez-Gómez, C., et al., 2021. Gas phase hydrogenation of furfural to obtain valuable products using commercial Cr-free catalysts as an environmentally sustainable alternative to copper chromite. Journal of Environmental Chemical Engineering. 9, 105468.

Lee, Y.-J., et al., 2021. Thermocatalytic oxidation of a three-component mixture of volatile organic compounds by a titanium dioxide-supported platinum catalyst. Journal of Cleaner Production. 325, 129279.

Li, J. W., et al., 2014. Removal of formaldehyde over $Mn_xCe_{1-x}O_2$ catalysts: Thermal catalytic oxidation versus ozone catalytic oxidation. Journal of Environmental Sciences. 26, 2546-2553.

Li, L., et al., 2015a. Supercapacitor electrodes based on hierarchical mesoporous MnOx/nitrided TiO2 nanorod arrays on carbon fiber paper. Advanced Materials Interfaces. 2, 1400446.

Li, R., et al., 2020. A Review of Co3O4-based Catalysts for Formaldehyde Oxidation at Low Temperature: Effect Parameters and Reaction Mechanism. Aerosol Science and Engineering. 4, 147-168.

Li, W., et al., 2015b. Facile synthesis of porous Mn_2O_3 nanocubics for high-rate supercapacitors. Electrochimica Acta. 157, 108-114.

Li, Y., et al., 2018. Sodium enhances Ir/TiO_2 activity for catalytic oxidation of formaldehyde at ambient temperature. ACS Catalysis. 8, 11377-11385.

667 Liu, L., et al., 2020. Enhanced catalytic oxidation of chlorobenzene over MnO_2 grafted in situ by rare earth oxide: surface
668 doping induces lattice oxygen activation. Inorganic Chemistry. 59, 14407-14414.
669 Liu, P., et al., 2016. Effect of Mn substitution on the promoted formaldehyde oxidation over spinel ferrite: Catalyst
670 characterization, performance and reaction mechanism. Applied Catalysis B: Environmental. 182, 476-484.
671 Liu, P., et al., 2019. The catalytic oxidation of formaldehyde over palygorskite-supported copper and manganese oxides:
672 Catalytic deactivation and regeneration. Applied Surface Science. 464, 287-293.
673 Liu, P., et al., 2018. Synergetic effect of Cu and Mn oxides supported on palygorskite for the catalytic oxidation of
674 formaldehyde: Dispersion, microstructure, and catalytic performance. Applied Clay Science. 161, 265-273.
675 Lu, S., et al., 2018. Ag–K/MnO_2 nanorods as highly efficient catalysts for formaldehyde oxidation at low temperature.
676 RSC advances. 8, 14221-14228.
677 Luengas, A., et al., 2015. A review of indoor air treatment technologies. Reviews in Environmental Science and
678 Bio/Technology. 14, 499-522.
679 Ma, L., et al., 2014. Ag/CeO_2 nanospheres: Efficient catalysts for formaldehyde oxidation. Applied Catalysis B:
680 Environmental. 148, 36-43.
681 Nielsen, G. D., et al., 2017. Re-evaluation of the WHO (2010) formaldehyde indoor air quality guideline for cancer risk
682 assessment. Archives of toxicology. 91, 35-61.
683 Nishikawa, A., et al., 2021. A comprehensive review of mechanistic insights into formaldehyde-induced nasal cavity
684 carcinogenicity. Regulatory Toxicology and Pharmacology. 123, 104937.
685 Onrubia-Calvo, J. A., et al., 2022. Kinetics, Model Discrimination, and Parameters Estimation of CO_2 Methanation on
686 Highly Active Ni/CeO_2 Catalyst. Industrial & Engineering Chemistry Research. 61, 10419-10435.
687 Perdew, J. P., et al., 1996. Generalized gradient approximation made simple. Physical review letters. 77, 3865.
688 Robert, B., Nallathambi, G., 2021. Indoor formaldehyde removal by catalytic oxidation, adsorption and nanofibrous

membranes: a review. Environmental Chemistry Letters. 19, 2551-2579.

Rudd, S., et al., 2022. Surface Doping in Poly (3, 4-ethylenedioxythiophene)-Based Nanoscale Films: Insights for Polymer Electronics. ACS Applied Nano Materials. 5, 12143-12153.

Saravanakumar, B., et al., 2017. Electrochemical properties of rice-like copper manganese oxide ($CuMn_2O_4$) nanoparticles for pseudocapacitor applications. Journal of Alloys and Compounds. 723, 115-122.

Sing, K. S., 1985. Reporting physisorption data for gas/solid systems with special reference to the determination of surface area and porosity (Recommendations 1984). Pure and applied chemistry. 57, 603-619.

Soler, J. M., et al., 2002. The SIESTA method for ab initio order-N materials simulation. Journal of Physics: Condensed Matter. 14, 2745.

Sun, D., et al., 2018. Ultrathin Bi_2WO_6 nanosheet decorated with Pt nanoparticles for efficient formaldehyde removal at room temperature. Applied Surface Science. 441, 429-437.

Sun, D., et al., 2019. Pt/C@MnO_2 composite hierarchical hollow microspheres for catalytic formaldehyde decomposition at room temperature. Applied Surface Science. 466, 301-308.

Thommes, M., et al., 2015. Physisorption of gases, with special reference to the evaluation of surface area and pore size distribution (IUPAC Technical Report). Pure and applied chemistry. 87, 1051-1069.

Troullier, N., Martins, J. L., 1991. Efficient pseudopotentials for plane-wave calculations. Physical review B. 43, 1993.

Tseng, L.-T., et al., 2015. Magnetic properties in α-MnO_2 doped with alkaline elements. Scientific reports. 5, 1-8.

Tu, S., et al., 2021. Complete catalytic oxidation of formaldehyde at room temperature on $Mn_xCo_{3-x}O_4$ catalysts derived from metal-organic frameworks. Applied Catalysis A: General. 611, 117975.

Vellingiri, K., et al., 2020. Advances in thermocatalytic and photocatalytic techniques for the room/low temperature oxidative removal of formaldehyde in air. Chemical Engineering Journal. 399, 125759.

Vetrimani, A., et al., 2022. Effect of green synthesized CuO plate-like nanoparticles in photodegradation and antibacterial

activities. Physical Chemistry Chemical Physics.

Vikrant, K., et al., 2019. Adsorption properties of advanced functional materials against gaseous formaldehyde. Environmental research. 178, 108672.

Vikrant, K., et al., 2022a. Deep oxidation of gaseous formaldehyde at room-temperature by a durable catalyst formed through the controlled addition of potassium to platinum supported on waste eggshell. Chemical Engineering Journal. 428, 131177.

Vikrant, K., et al., 2022b. Low-temperature oxidative removal of gaseous formaldehyde by an eggshell waste supported silver-manganese dioxide bimetallic catalyst with ultralow noble metal content. Journal of Hazardous Materials. 434, 128857.

Vikrant, K., et al., 2022c. Harnessing Adsorption–Catalysis Synergy: Efficient Oxidative Removal of Gaseous Formaldehyde by a Manganese Dioxide/Metal–Organic Framework Nanocomposite at Room Temperature. Advanced Functional Materials. 2107922.

Vikrant, K., et al., 2021. Platinized titanium dioxide (Pt/TiO_2) as a multi-functional catalyst for thermocatalysis, photocatalysis, and photothermal catalysis for removing air pollutants. Applied Materials Today. 23, 100993.

Vikrant, K., et al., 2023. Two-dimensional titanium carbide (MXene)-supported Pt_3Ti intermetallic compound catalysts for efficient room-temperature oxidative removal of gaseous formaldehyde. Materials Today Nano. 21, 100283.

Vyazovkin, S., 2021. Determining preexponential factor in model-free kinetic methods: how and why? Molecules. 26, 3077.

Wan, C., et al., 2017. A cellulose fibers-supported hierarchical forest-like cuprous oxide/copper array architecture as a flexible and free-standing electrode for symmetric supercapacitors. Journal of Materials Chemistry A. 5, 17267-17278.

Wang, C., et al., 2018a. Synthesis of palygorskite-supported $Mn_{1-x}Ce_xO_2$ clusters and their performance in catalytic

733 oxidation of formaldehyde. Applied Clay Science. 159, 50-59.

734 Wang, F., et al., 2022. Copper-manganese oxide for highly selective oxidation of 5-hydroxymethylfurfural to bio-
735 monomer 2, 5-furandicarboxylic acid. Biomass Conversion and Biorefinery. 1-12.

736 Wang, J., et al., 2018b. Preparation of nanostructured Cu $(OH)_2$ and CuO electrocatalysts for water oxidation by
737 electrophoresis deposition. Journal of Materials Research. 33, 581-589.

738 Wang, X., et al., 2017. Structure–Activity Relationships of AMn_2O_4 (A = Cu and Co) Spinels in Selective Catalytic
739 Reduction of NO_x: Experimental and Theoretical Study. The Journal of Physical Chemistry C. 121, 3339-3349.

740 Wang, Y., et al., 2019. Layered copper manganese oxide for the efficient catalytic CO and VOCs oxidation. Chemical
741 Engineering Journal. 357, 258-268.

742 Wang, Z., et al., 2020. Experimental and DFT studies of the role of H_2S in Hg_0 removal from syngas over $CuMn_2O_4$
743 sorbent. Chemical Engineering Journal. 391, 123616.

744 Weina, X., et al., 2017. A novel β-MnO_2 micro/nanorod arrays directly grown on flexible carbon fiber fabric for high-
745 performance enzymeless glucose sensing. Electrochimica Acta. 225, 121-128.

746 Wu, P., et al., 2021. Recent Progress of Thermocatalytic and Photo/Thermocatalytic Oxidation for VOCs Purification
747 over Manganese-based Oxide Catalysts. Environmental Science & Technology. 55, 4268-4286.

748 Xu, L., et al., 2019. In situ growth of Cu_2O/CuO nanosheets on Cu coating carbon cloths as a binder-free electrode for
749 asymmetric supercapacitors. Frontiers in chemistry. 7, 420.

750 Yang, Y., et al., 2019. Reaction mechanism for NH_3-SCR of NO_x over $CuMn_2O_4$ catalyst. Chemical Engineering Journal.
751 361, 578-587.

752 Yi, Y., et al., 2018. The synthetic evaluation of CuO-MnO_x-modified pinecone biochar for simultaneous removal
753 formaldehyde and elemental mercury from simulated flue gas. Environmental Science and Pollution Research.
754 25, 4761-4775.

Yoo, M.-J., et al., 2019. An advanced technique for rapid and accurate monitoring of gaseous formaldehyde using large-volume injection interfaced with gas chromatograph/barrier discharge ionization detector (LVI/GC/BID). Microchemical Journal. 147, 806-812.

Zhang, C., et al., 2006. Catalytic performance and mechanism of a Pt/TiO_2 catalyst for the oxidation of formaldehyde at room temperature. Applied Catalysis B: Environmental. 65, 37-43.

Zhang, C., et al., 2021. $CuMn_2O_4$ spinel anchored on graphene nanosheets as a novel electrode material for supercapacitor. Journal of Energy Storage. 34, 102181.

Zhang, Y., et al., 2022. Synergically engineering Cu+ and oxygen vacancies in CuMn2O4 catalysts for enhanced toluene oxidation performance. Molecular Catalysis. 517, 112043.

Zhao, L., et al., 2022. Mechanistic insights into benzene oxidation over CuMn2O4 catalyst. Journal of Hazardous Materials. 431, 128640.

Zhao, Q., et al., 2017. Spinels: Controlled Preparation, Oxygen Reduction/Evolution Reaction Application, and Beyond. Chemical Reviews. 117, 10121-10211.

Zhu, L., et al., 2017. Cerium modified birnessite-type MnO2 for gaseous formaldehyde oxidation at low temperature. Applied Catalysis B: Environmental. 211, 212-221.

Zhu, S., et al., 2019. Progress of catalytic oxidation of formaldehyde over manganese oxides. ChemistrySelect. 4, 12085-12098.

Tables and Figures

Table 1. Physical characteristics of the analyzed catalysts.

Order	Materials	BET surface area ($m^2\ g^{-1}$)	Pore volume ($cm^3\ g^{-1}$)	BJH Average pore diameter (Å)	Actual content (wt. %)[a]	
					Cu	Mn
1	$Cu_{0.5}Mn_2O_4$	16.23	0.026	48.21	18.89	63.74
2	$CuMn_2O_4$	21.66	0.036	47.11	31.42	51.50
3	$Cu_2Mn_2O_4$	8.11	0.011	41.97	46.12	43.58

[a] Determined by ICP-OES.

Table 2. Surface composition of the studied catalysts based on XPS analysis.

Order	Material	Cu 2*p*			Mn 2*p*			O *1s*		
		Species	Peak Position (eV)	Cu^{2+} content[a] (%)	Species	Peak Position (eV)	Mn^{4+} content[b] (%)	Species	Peak Position (eV)	O_A content[c] (%)
1	$Cu_{0.5}Mn_2O_4$-O	$2p_{3/2}$ Cu^+	931.1	66.8	$2p_{3/2}$ Mn^{3+}	641.7	40.0	O_L	529.8	42.4
		$2p_{3/2}$ Cu^{2+}	933.9							
		$2p_{1/2}$ Cu^+	950.9		$2p_{3/2}$ Mn^{4+}	643.6		O_A	531.0	
		$2p_{1/2}$ Cu^{2+}	953.7							
2	$Cu_{0.5}Mn_2O_4$-R	$2p_{3/2}$ C^0&Cu^+	932.9	50.5	$2p_{3/2}$ Mn^{3+}	641.4	31.2	O_L	530.0	41.3
		$2p_{3/2}$ Cu^{2+}	933.7							
		$2p_{1/2}$ C^0&Cu^+	952.7		$2p_{3/2}$ Mn^{4+}	643.8		O_A	531.3	
		$2p_{1/2}$ Cu^{2+}	953.6							
3	$CuMn_2O_4$-O	$2p_{3/2}$ Cu^+	931.0	72.2	$2p_{3/2}$ Mn^{3+}	641.5	52.7	O_L	529.8	47.2
		$2p_{3/2}$ Cu^{2+}	933.7							
		$2p_{1/2}$ Cu^+	950.8		$2p_{3/2}$ Mn^{4+}	643.9		O_A	531.0	
		$2p_{1/2}$ Cu^{2+}	953.5							
4	$CuMn_2O_4$-R	$2p_{3/2}$ C^0&Cu^+	932.7	42.8	$2p_{3/2}$ Mn^{3+}	641.4	45.1	O_L	530.0	44.9
		$2p_{3/2}$ Cu^{2+}	933.8							
		$2p_{1/2}$ C^0&Cu^+	952.6		$2p_{3/2}$ Mn^{4+}	643.6		O_A	531.2	
		$2p_{1/2}$ Cu^{2+}	953.7							
5	$Cu_2Mn_2O_4$-O	$2p_{3/2}$ Cu^+	930.9	64.2	$2p_{3/2}$ Mn^{3+}	641.6	38.1	O_L	529.8	43.1
		$2p_{3/2}$ Cu^{2+}	933.5							
		$2p_{1/2}$ Cu^+	950.8		$2p_{3/2}$ Mn^{4+}	643.9		O_A	531.0	
		$2p_{1/2}$ Cu^{2+}	953.4							
6	$Cu_2Mn_2O_4$-R	$2p_{3/2}$ C^0&Cu^+	932.6	47.9	$2p_{3/2}$ Mn^{3+}	641.4	31.2	O_L	529.9	40.4
		$2p_{3/2}$ Cu^{2+}	933.6							
		$2p_{1/2}$ C^0&Cu^+	952.5		$2p_{3/2}$ Mn^{4+}	643.8		O_A	531.2	
		$2p_{1/2}$ Cu^{2+}	953.4							

[a] Cu^{2+} content was estimated as $Cu^{2+}/[Cu^{2+}+ (Cu^+ \text{ or } Cu^0 + Cu^+)]\times100\%$.

[b] Mn^{4+} content was estimated as $Mn^{4+}/[Mn^{4+} + Mn^{3+}]\times100\%$.

[c] O_A content was estimated as $O_A/[O_A + O_L] \times100\%$.

Table 3. FA oxidation performance of the tested catalysts[a]

Order	Catalysts	T_{50}[d]	T_{90}[d]	Maximum X_{FA} (%) at 90℃	r (mmol g_{cat}^{-1} h^{-1}) at maximum X_{FA} at 90°C
1	$Cu_{0.5}Mn_2O_4$-O[b]	73	100	66	2.77E-02
2	$Cu_{0.5}Mn_2O_4$-R[c]	84	103	57	2.39E-02
3	$CuMn_2O_4$-O	51	85	100	4.19E-02
4	$CuMn_2O_4$-R	72	93	87	3.65E-02
5	$Cu_2Mn_2O_4$-O	86	102	58	2.43E-02
6	$Cu_2Mn_2O_4$-R	91	108	46	1.93E-02

[a] Reactant composition: FA (50 ppm) + air (balance), flow rate: 50 mL min^{-1} (1.40E-09 mol s^{-1}), catalyst mass (120 mg), and GHSV (3,979 h^{-1}).

[b] 'O' indicates oxidative pre-treatment using air gas at 300°C for 3 h (50 mL min^{-1}).

[c] 'R' indicates reduction pre-treatment using H_2 (10%) + N_2 at 300°C for 3 h (50 mL min^{-1}).

[d] T_{50} and T_{90} are the reaction temperatures corresponding to 50% and 90% X_{FA}, respectively.

837 **Table 4.** Performance comparison between analyzed $CuMn_2O_4$ catalysts and other common catalysts for FA catalytic oxidation.

838

Order	Catalyst	Catalyst activation	m_{cat} (mg)	Reactant mixture	FA concentration (ppm)	Flow rate (mL min^{-1})	Flow rate (mol s^{-1}) at T_{10}	Flow rate (mol s^{-1}) at maximum X_{FA} at 90 °C	Space velocity	T_{50}[c] (°C)	T_{90}[c] (°C)	r (mmol g_{cat}^{-1} h^{-1})[a] at 10% X_{FA}	T_{10} (°C)	Maximum X_{FA} (%) at 90°C	r (mmol g_{cat}^{-1} h^{-1})[a] at maximum X_{FA} at 90°C	Reference
1	β-MnO_2	NA	200	400 ppm FA+20% O_2+ N_2	400	100	2.04 E-08	2.24E-08	30,000 mL. g^{-1} h^{-1}	146	165	3.67 E-02	125	1	4.02E-03	(Bai et al., 2016b)
2	Nano Co_3O_4	NA	200	400 ppm FA + 20%O_2+N_2	400	100	1.77 E-08	2.24E-08	30,000 mL. g^{-1} h^{-1}	210	225	3.19 E-02	185	1	4.02E-03	(Bai et al., 2013)
3	CeO_2	NA	200	50 ppm FA + 25%O_2+ N_2	50	100	2.72 E-09	2.80E-09	30,000 mL. g^{-1} h^{-1}	170	250	4.90 E-03	100	8	4.02E-03	(Huang et al., 2016)
4	3D-MnO_2	NA	200	400 ppm FA+20% O_2+ N_2	400	100	2.44 E-08	2.24E-08	30,000 mL. g^{-1} h^{-1}	94	110	4.39 E-02	60	38	1.53E-01	(Bai et al., 2016b)
5	2D-Co_3O_4	NA	200	400 ppm FA + 20%O_2+N_2	400	100	2.18 E-08	2.24E-08	30,000 mL. g^{-1} h^{-1}	122	140	3.92 E-02	100	8	3.22E-02	(Bai et al., 2013)
6	$Mn_{0.5}Ce_{0.5}O_2$	NA	300	33 ppm FA+21%O_2 +Air	33	600	1.05 E-08	1.11E-08	10,000 h^{-1}	160	250	1.26 E-02	110	10	1.33E-02	(Li et al., 2014)
7	$Mn_{1-x}Ce_xO_2$/palygorskite	NA	100	300 ppm FA+Air	300	100	NA	1.68E-08	20,000 h^{-1}	140	156	NA	NA	NA	NA	(Wang et al., 2018a)

8	Ag-1.5%-MnO_2-Eggshell	Reduction at 300 °C using H_2 (10%) + N_2 mixture for 3 h (50 mL min^{-1})	120	FA + Air (balance)	100	50	NA	2.80E-09	5308 h^{-1}	< 30 (62% XFA at 30 °C)	77	NA	NA	96	8.05E-02	(Vikrant et al., 2022b)
9	Ag-0.9%-K-MnO_2	Reduction at 200 °C using H_2 (10%) + N_2 mixture for 1 h	50	FA + O_2 (21 vol%) + N_2 (balance)	300	30	NA	5.03E-09	3600 mL h^{-1} g^{-1}	< 20 (70% XFA at 20 °C)	35	NA	NA	100	3.62E-01	(Lu et al., 2018)
10	Ag-CeO_2	NA	50	FA + O_2 (20 vol%) + N_2 (balance)	810	100	5.09 E-08	4.53E-08	8400 h^{-1}	90	10 8	3.66 E-01	50	46	1.50E+00	(Ma et al., 2014)
11	$CuMn_2O_4$-O	Oxidation at 300 °C using Air for 3 h (50 mL min^{-1})	50	FA + Air (balance)	50	50	1.67 E-09	1.40E-09	3,979 h^{-1}	51	85	5.02 E-03	20[b]	100	4.19E-02	This work

[a] Calculated using Equation 3. The calculated values are only used for FA oxidation performance comparison (Section 3.6). When the reactors operate in the integral mode (X_{FA} > 20%),

the values calculated using Equation 3 may overestimate the true r. As the governing rate expression, kinetic parameters, and other details for the reported catalysts may not be available, a simplified r calculation using Equation 3 was favored for catalytic FA oxidation performance comparison purposes. Note that the calculated r values should not be treated as the real r under the specified conditions when the reactors operated in the integral mode (X_{FA} > 20%). [b] the temperature for obtaining r value at X_{FA}=10% is estimated at 20℃. [c] T_{50} and T_{90} are the reaction temperatures corresponding to 50% and 90% X_{FA}, respectively.

839

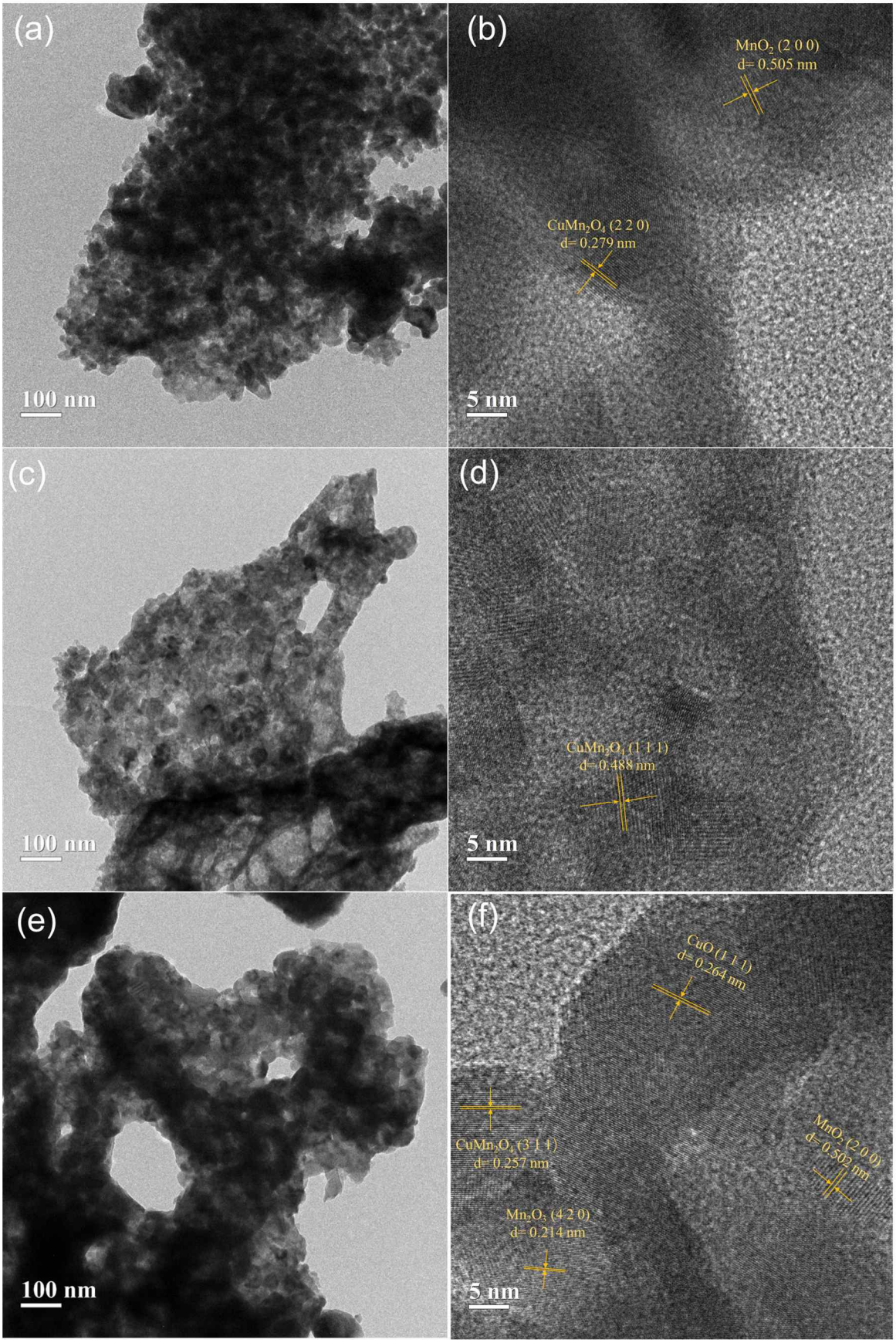

Figure 1. TEM images of the tested catalysts. (a-b) $Cu_{0.5}Mn_2O_4$, (c-d) $CuMn_2O_4$, and (e-f) $Cu_2Mn_2O_4$.

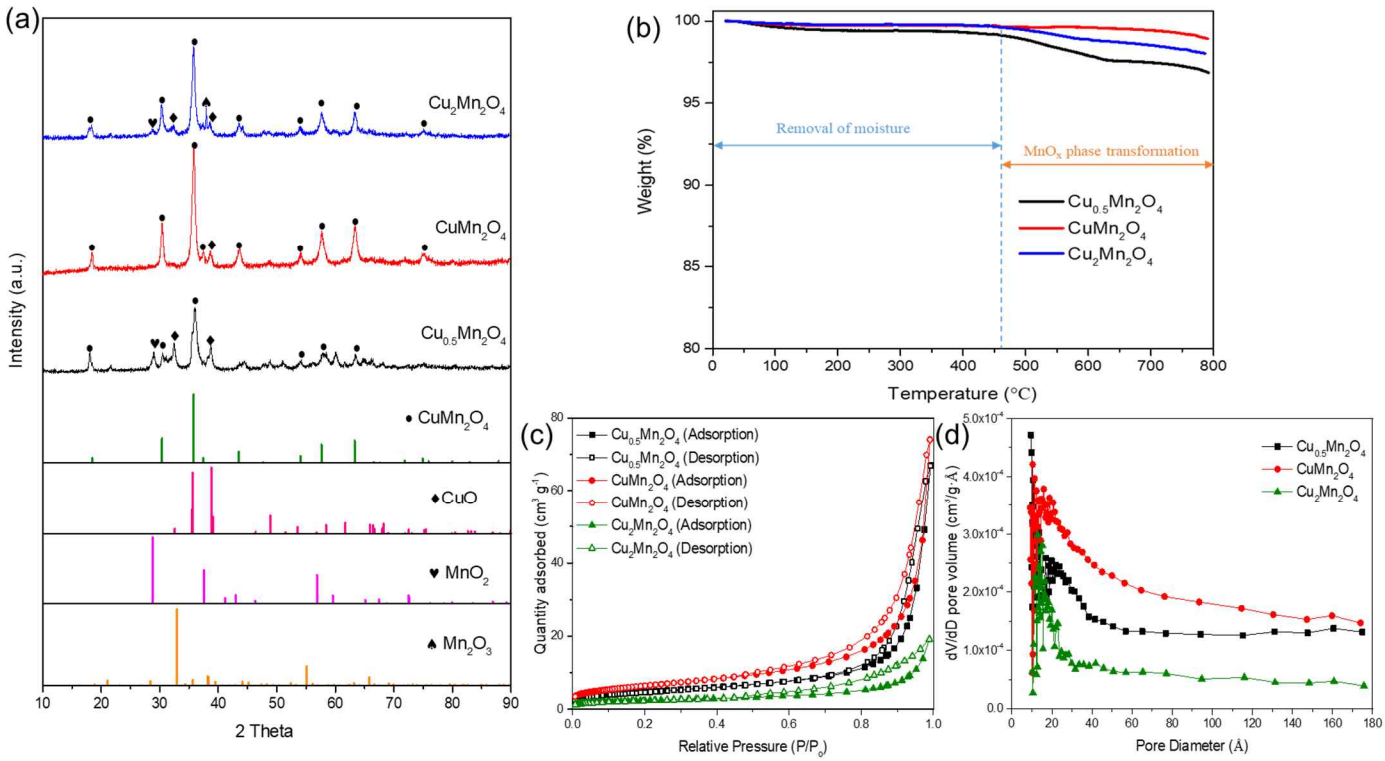

Figure 2. Characterization results of the tested materials: (a) PXRD patterns, (b) TGA analysis, (c) N_2 adsorption-desorption isotherms, and (d) Pore size distributions.

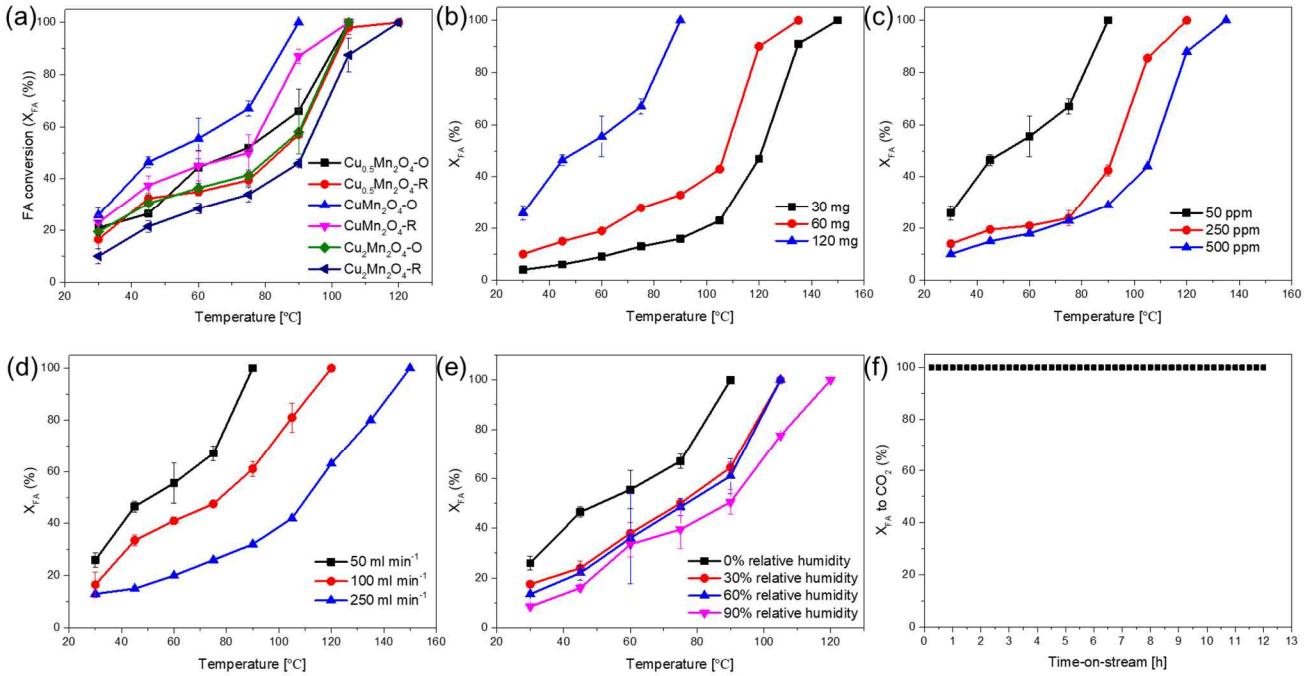

Figure 3. FA removal performance of the analyzed catalysts. (a) Light-off curves (FA: 50 ppm in air, m_{cat}: 120 mg, flow rate: 50 ml min^{-1}, and RH: 0%), (b) Effect of m_{cat} (catalyst: $CuMn_2O_4$-O, FA: 50 ppm in air, flow rate: 50 ml min^{-1}, and RH: 0%), (c) Effect of FA concentration (catalyst: $CuMn_2O_4$-O, m_{cat}: 120 mg, flow rate: 50 ml min^{-1}, and RH: 0%), (d) Effect of flow rate (catalyst: $CuMn_2O_4$-O, FA: 50 ppm in air, m_{cat}: 120 mg, and RH: 0%), (e) Effect of RH (catalyst: $CuMn_2O_4$-O, FA: 50 ppm in air, m_{cat}: 120 mg, and flow rate: 50 ml min^{-1}), and (f) TOS performance of $CuMn_2O_4$-O at 90 □ (FA: 50 ppm in air, flow rate: 50 ml min^{-1}, m_{cat}: 120 mg, and RH: 0%). Error bars represent standard deviation of two runs.

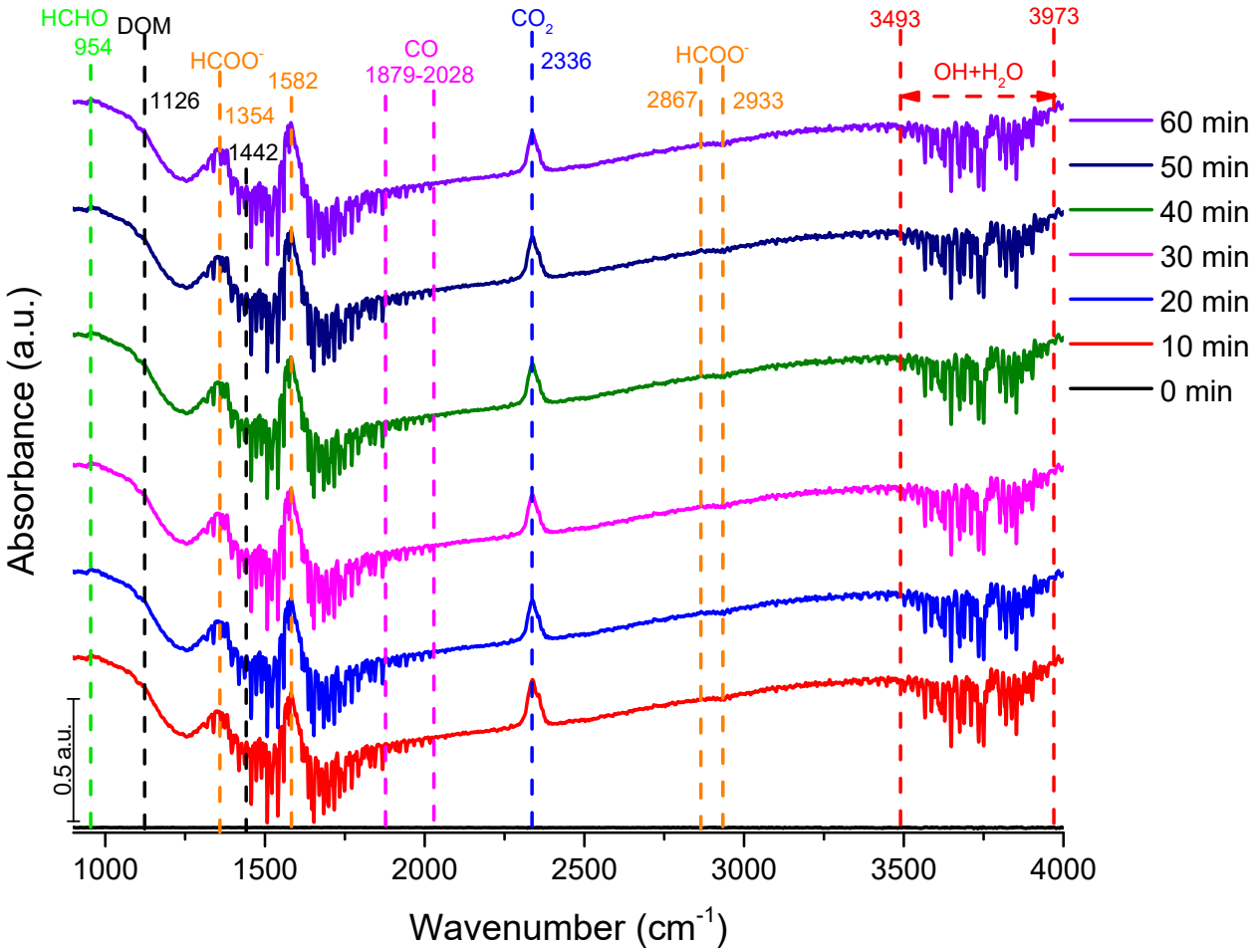

Figure 4. *In-situ* DRIFTS spectrum (acquired at 90°C in the dark) for $CuMn_2O_4$-O (FA + air mixture).

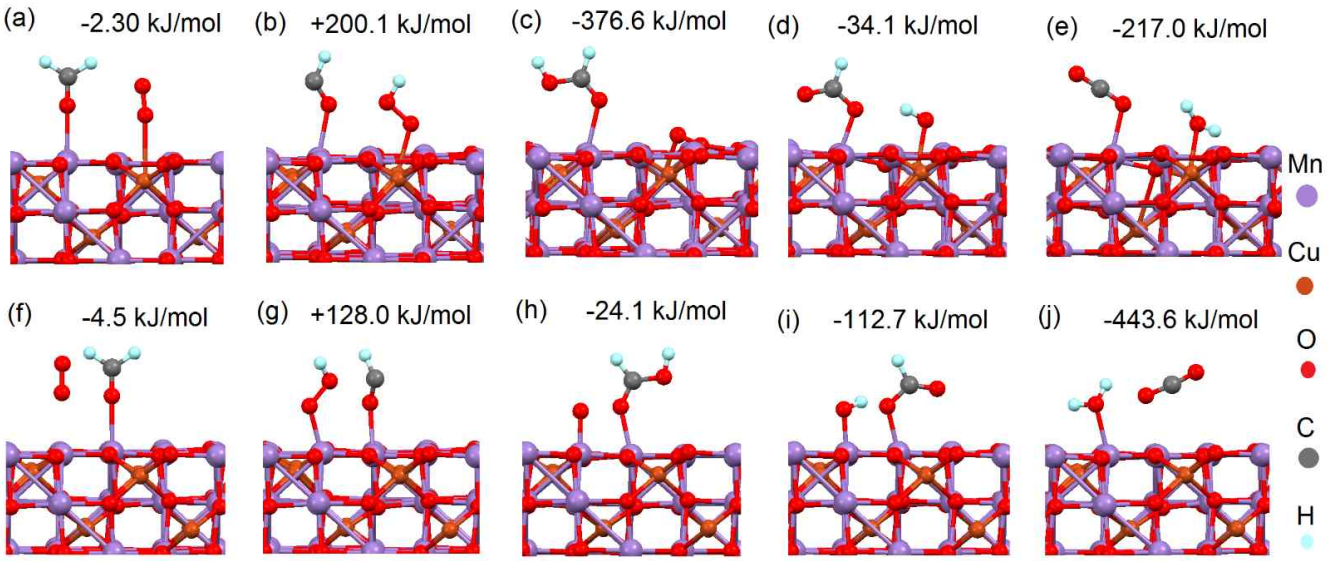

Figure 5. Optimized atomic structures and corresponding free energies for X_{FA} over the $CuMn_2O_4$ substrate: (a, f) initial, (b-d, g-i)intermediate, and (e, j) final steps of two simulated pathways (both manganese and copper and only manganese on the surface of catalyst substrate) .